POLITECNICO MILANO 1863

DIPARTIMENTO DI MECCANICA

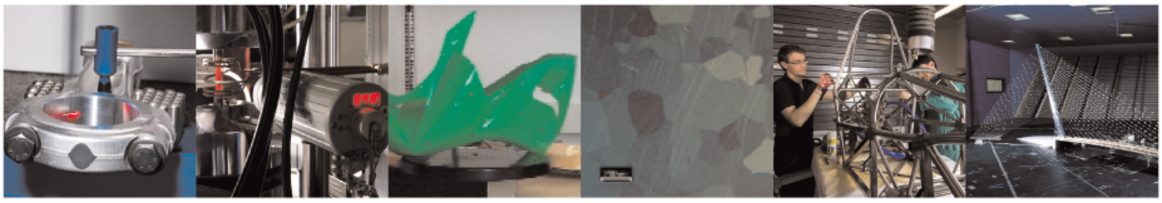

Orientation-dependent fatigue assessment of Ti6Al4V manufactured by L-PBF: size of surface features and shielding effect

Barricelli, L.;Patriarca, L.;du Plessis, A.;Beretta, S.

This is a post-peer-review, pre-copyedit version of an article published in International Journal of Fatigue. The final authenticated version is available online at: https://doi.org/10.1016/j.ijfatigue.2022.107401

DIPARTIMENTO DI MECCANICA ■ POLITECNICO DI MILANO
via G. La Masa, 1 ■ 20156 Milano ■ EMAIL (PEC): pecmecc@cert.polimi.it
http://www.mecc.polimi.it
Rev. 0

Orientation-dependent fatigue assessment of Ti6Al4V manufactured by L-PBF: size of surface features and shielding effect

L. Barricelli[a], L. Patriarca[a], A. du Plessis[b,c], S. Beretta[a,*]

[a] *Politecnico di Milano, Department of Mechanical Engineering, Via La Masa 1, I-20156 Milan, Italy*
[b] *Research group 3D Innovation, Physics Department, Stellenbosch University, Stellenbosch 7602 South Africa*
[c] *Object Research Systems, Montreal, Quebec H3B 1A7, Canada*

Abstract

The fatigue behaviour of as-built parts produced by means of Laser-Powder Bed Fusion process (L-PBF) is primarily influenced by the presence of stress raisers on the surface, whose morphology strongly depends on the relative orientation between the surface and the build direction. This study aims to shed light into the factors representing the surface morphology that correlate with the fatigue performance of L-PBF Ti6Al4V specimens manufactured in four different orientations. A Fracture Mechanics-based model based on measurable roughness parameters was employed for the prediction of the fatigue properties in both the finite life and endurance limit regions. The fatigue model considers an initial equivalent defect corresponding to the roughness parameter $R_{v,max}$. In addition, it includes a geometric factor $\overline{F}$ accounting for the shielding present at the roots of the micro-notches which was calculated starting from profile roughness parameters determined by X-ray Computer Tomography (XCT) scans. The predicted stress-life curves show that the adoption of the maximum profile depth $R_{v,max}$ and the shielding factor $\overline{F}$ yields precise life predictions considering the effect of the surface orientation.

Keywords: Ti6Al4V, Additive Manufacturing, L-PBF, roughness, as-built, fatigue, Fracture Mechanics, life prediction

* Corresponding author
Email address: stefano.beretta@polimi.it (S. Beretta)

Abbreviations

The following abbreviations are used in this manuscript:

2D - Two dimension

3PB - 3-Point Bending

4PB - 4-Point Bending

AM - Additive Manufacturing

CA - Constant Amplitude

EIFS - Equivalent Initial Flaw Size

EBM - Electron-beam melting

EDM - Electrical Discharge Machining

FCG - Fatigue Crack Growth

FE - Finite Element

HIP - Hot Isostatic Pressing

LEVD - Largest Extreme Value Distribution

LOF - Lack of Fusion

L-PBF - Laser-Powder Bed Fusion process

LR - Load Reduction

LS - Least Squares

SEB - Single Edge Bending

SEM - Scanning Electron Microscope

SIF - Stress Intensity Factor

Ti - Titanium

UTS - Ultimate Tensile Stress

XCT - X-ray Computer Tomography

Nomenclature

$\sqrt{10}R_{v,max}$ - Equivalent crack size from the profile roughness parameter $R_{v,max}$

$\sqrt{10}t$ - Equivalent crack size from the killer defect's depth t

$\sqrt{area}$ - Murakami's equivalent crack size, square root of the defect area

$\sqrt{area}_0$ - El-Haddad parameter in terms of $\sqrt{area}$

$\sqrt{area}_{50\%}$ - Murakami's equivalent crack size at the 50% probability of the LEVD

$\sqrt{area}_R$ - Murakami's parameter for the roughness

α - Constraint parameter of NASGRO equations

δ - LEVD scale parameter

$\Delta\sigma$ - Applied stress range

$\Delta\sigma_{w,0}$ - theoretical endurance limit range of the defectless alloy

$\Delta\sigma_{w,exp}$ - Experimental fatigue limit range

ΔK - SIF range

ΔK_I - Mode I SIF range

$\Delta K_{th,LC}$ - Long Crack Threshold SIF range

$\overline{\lambda}$ - Profile wavelengths

λ - LEVD location parameter

λ_c - Profile cut-off wavelength

ϵ_U - Ultimate Tensile Strain

σ - LEVD standard deviation of data

σ_0 - Applied remote stress

σ_{logN} - Standard deviation of the fatigue data in the finite-life regime

σ_{max}/σ_O - Ratio between the maximum stress and the flow stress

μ - LEVD mean of data

a - Crack depth

a_0 - Small crack parameter

$A_{0,1,2,3}$ - Parameters of Newman's crack closure function

A, B - Parameters of the S-N curve in the finite-life regime

a_n - Initial notch length of SEB specimens

b - Crack pitch

c - Crack semi-width

C, m, p, q - NASGRO fitting parameters for the FCG curves

C_{th}^m,C_{th}^p, ΔK_I^* - NASGRO fitting parameters for the Long Crack threshold

$(c/a)_{in}$ - Crack aspect ratio, initial

da/dN - Crack propagation rate

E - Young Modulus

f - Newman's crack closure function

$\overline{F}$ - Average shielding factor

F_{LEVD} - LEVD cumulative density function

i - Profile section pedix

l_s - Profile sampling length

K_I - Mode I SIF

K_c - Fracture toughness

N - Number of cycles

N_{lim} - Fatigue life, number of fatigue cycles at the S-N knee-point

R - Stress Ratio

R_a, S_a - Arithmetic mean roughness (profile, areal)

R_c - Mean height of profile features

R_{pc} - Profile peak counts

$R_{p,i}$ - Section peak height

$R_{p,m}$ - Mean profile peak height

$R_{p,max}$ - Maximum profile peak height

R_{sm} - Mean width of profile elements

$R_{sm,i}$ - Mean width of section elements

R_t - Total height of profile elements

$R_{v,i}$ - Section valley depth

$R_{v,m}$ - Mean profile valley depth

$R_{v,max}$, S_v - Maximum valley depth (profile, areal)

S_{dq} - root mean square surface slope

S_{Sk} - skewness areal parameter

S_y - Yielding Stress

S-N - Stress-Life (Wöhler) curves

t - Killer defect's depth

t_{max} - Maximum groove depth of an as-built profile

w - Killer defect's width

w/t - Killer defect's aspect ratio

Y - Murakami's boundary correction factor

1. Introduction

The large diffusion of Ti6Al4V alloy for Additive Manufacturing (AM) applications is well justified by its outstanding material properties, i.e. excellent ratio between static mechanical properties and density, good corrosion resistance, excellent weldability and bio-compatibility. These properties make the Ti6Al4V alloy very captivating for the aerospace [1, 2] and medical industries [2, 3], especially in relation to the additive manufacturing processes. In this regard, it is observed that the static properties of Ti6Al4V alloys manufactured by means of Laser-Powder Bed Fusion process (L-PBF) are comparable with those of wrought Ti alloys [4, 5]. On the other hand, the fatigue performance of Ti6Al4V L-PBF parts has been observed to be reduced and subjected to a larger variability due to the presence of stress raisers introduced by the manufacturing process, i.e. internal defects and surface anomalies [6]. A wider adoption of the Ti6Al4V alloy in the AM industry requires a further improvement on the capability to predict the fatigue performance of AMed parts and the key factors affecting it. This work aims to shed light into the effect of the surface orientation on the fatigue behavior of the Ti6Al4V alloy correlating measurable surface roughness parameters with the fatigue life in a fracture mechanics-based framework.

Among all the factors that influence the morphology of the as-built surface, the process-window, the locational dependency and the inclination of the surface with respect to the build plate are considered the most important ones. The as-built surface morphology is primarily influenced by the volumetric energy density [7] and thus, in the case of the L-PBF process, by the laser power and scan speed. The second important factor for the surface quality is the locational dependency. Two parts of the same build may have a different surface quality depending on their position on the build plate and when lacking uniformity of the shielding gas within the build chamber [8, 9]. The third main factor is the build orientation which has a strong impact on the surface morphology [10, 11]. Overhang surfaces of as-built L-PBF parts with intermediate inclination angles between the horizontal and the vertical orientations have a complex surface that results from the combination of the layer stratification (stair-case effect), the melt pool dynamics and the melting-solidification mechanisms that occur as the metal interacts with the laser beam during printing, with an influence of the local heat conductivity, surface tension and gravity on the final surface shape [10–14].

In the view of a process-structure-property understanding, the characterization of as-built overhang surfaces is a key factor as demonstrated by recent published works [14–17]. Currently, an open point is what surface parameter can properly describe the surface morphology and, at the same time, correlate with the fatigue behaviour. The ideal roughness parameter should be able to distinguish among the different surface qualities at different build angles, as the downskin surfaces (those facing the build plate during printing) have the worst impact on fatigue properties of as-built L-PBF parts [11, 18–20].

The average roughness parameter R_a has been investigated by Persenot et al. [21], who could not find any correlation of such parameter with the fatigue life. Indeed, other works show that R_a does not give enough information to distinguish different surface morphologies [7, 15, 22]. A maximum-height parameter (like the profile R_t or the areal S_z) is often found in literature as an equivalent initial defect that can be adopted as an input for life predictions based on the fracture mechanics theory, assuming the crack shape as semi-circular [6, 23] or 2D [24–26], providing good results but still retaining some uncertainties in the fatigue model. For instance, Greitemeier et al. [23] classified the laser tracks-dominated and the adhered particles-dominated surface morphologies as "primary" and "secondary" roughness, respectively, and adopted the parameter R_t (maximum profile height, measured with a contact stylus along the loading direction) as the Equivalent Initial Flaw Size (EIFS) in a fracture mechanics model to predict with good results the life of as-built L-PBF and EBM axial flat Ti6Al4V specimens. On the other side, Persenot et al. [21] observed that a global parameter like R_t may overlook some local stress raisers. In their work, the parameter R_t measured from radial XCT (X-ray Computed Tomography) sections of thin as-built (Electron Beam Melting) EBM Ti6Al4V cylindrical specimens printed at 0°, 45° and 90° was not representative of the "plate-pile" killer defects (very sharp notches perpendicular to the build orientation). Nonetheless, R_t parameter may still be worth being analyzed in order to include the impact of the locational dependency. Lee et al. [9] found that specimens that are located far from the gas inlet tend to have higher R_t values.

Among the others, the best parameter for the fatigue assessment seems to be the maximum profile or areal depth (R_v for 2D profiles, S_v for 3D areal roughness measurements). The maximum valley depth is consistent with the analysis of surface features as initial defects [24, 27] and the parameter R_v is found to correlate well with the fatigue behaviour of AM parts [28–32]. This confirms the evidence that the protrusions of a rough surface do not carry any load during fatigue testing, while the fatigue failure is enhanced by local stress concentrations that arise at the surface valleys or at sub-surface anomalies [33, 34].

A summary of the roughness parameters adopted for fracture mechanics-based fatigue predictions in recent literature is presented in Table 1. The table also shows the references that adopted a shielding factor in addition to the roughness parameter. The presence of multiple valleys could mitigate the stresses on the critical defect, and this effect is commonly referred to shielding. Barricelli and Beretta [35] performed FE analyses on 2D diametrical sections extracted from the XCT 3D reconstruction of as-built L-PBF cylindrical specimens to extract the SIF at the "critical valleys". They showed that the maximum valley depth can be adopted to predict the fatigue limit only if it is corrected by a proper shielding factor that accounts for the interaction of surface valleys that are close to each other.

Table 1: Roughness parameters adopted in literature as initial crack size in a Fracture Mechanics fatigue model

Author	**Year**	**Material**	**Crack shape**	**Parameter**	**Shielding**
Murakami [24]	1996	Steels	2D	S_z	yes
Wycisk et al. [6]	2014	Ti6Al4V	semi-circular	R_t	
Greitemeier et al. [23]	2015	Ti6Al4V	semi-circular	R_t	
Molaei et al. [25]	2019	Ti6Al4V	2D	R_t	yes
Nakatani et al. [26]	2019	Ti6Al4V	2D	S_z	yes
Chan [28]	2015	Ti6Al4V	semi-circular	R_v	
Zhang, Fatemi [29]	2019	Ti6Al4V	semi-circular/2D	R_v	yes
DuPlessis, Beretta [32]	2021	Ti6Al4V	2D	R_v	

Based on the evidence found in literature, in this paper we adopted the roughness parameter R_v as the initial equivalent defect together with a shielding factor. With particular focus on the latter parameter, we also propose a clear methodology to define an average shielding factor based on average roughness parameters which considers the orientation-dependence of the as-built surfaces.

The adoption of a crack propagation algorithm to perform life predictions requires an initial calibration from know initial defect sizes. Currently, an unclear aspect when investigating the killer notches of an as-built surface is how to properly measure the killer defect's $\sqrt{area}$ on the fracture surfaces. There are no clear guidelines in literature according to the author's knowledge. In this regard, in this paper we highlight a new method to measure the killer defect's size from the fracture surfaces. Solving this open point aims to reduce the scatter in predicting the fatigue properties due to inherent surface defect sizes and morphology [36]. In addition, the proposed methodology could support the identification of the killer notch's position from a 3D reconstruction of the surface, i.e. identifying among the several notches within the surface which is the most critical one that leads to the final failure. Among the few works treating this problem, it is worth citing those by Persenot et al. [37], adopting a systematic approach for the killer notches recognition based on the unfolding and binarisation of the XCT 3D cylindrical surface, and by Mian et al. [38], chosing a "visual local" approach to spot the "critical valleys" (a number of valleys among the deepest ones) within 2D profiles acquired by contact stylus along the loading direction of as-built dog-bone specimens. In this work we are adopting a visual analysis of the 3D reconstruction from XCT of the loaded surface of the specimen to spot the killer defect position and we are making reference to a fitting plane of the surface points to measure the notch size.

We note that for the present Ti6AL4V alloy the residual stresses were relieved by proper heat treatments, therefore the denomination "as-built" is herein referred to the sole surface condition. The internal porosity was not considered since the dominant effect was induced by the surface features.

The work is structured as follows:

- *Section 2* outlines the details of the experimental campaign.
- *Section 3* reports the results of the fatigue and the fatigue crack growth tests for the different series of specimens and the results of the roughness measurements.
- *Section 4* outlines the measurement method that yields the equivalent $\sqrt{area}$ in a Fracture Mechanics approach.
- *Section 5* illustrates the adopted fatigue limit model and the crack propagation algorithms for the fatigue life predictions.

2. Materials and experiment

2.1. Specimen manufacturing and heat treatment

The experimental campaign performed in the present study (Table 2) considered fatigue crack growth (FCG) tests for two specimen orientations and high cycle fatigue tests on axial and bending specimens for four orientations. The layout of the building plate is given in Figure 1, while the technical drawings of the specimens are detailed in Figure 2.

The Single Edge Bend (SEB) specimens for the FCG tests were manufactured as solid parallelepipeds (rectangular cross section) in both vertical and horizontal orientations (parallel and perpendicular to the build direction, respectively). The lateral surfaces of the SEB specimens were milled to guarantee the tolerances on the parallelism and perpendicularity required for testing under pure bending. Successively, a starter notch was obtained by means of Electrical Discharge Machining (EDM).

The cylindrical specimens for axial fatigue were built in vertical orientation, while the specimens for four-Point Bending Tests (4PB) were printed in 3 different orientations with respect to the build plate: 0° (horizontal), 45° and 135°. The latter two orientations were studied to assess the effect of the down-skin and the up-skin surface orientations on the fatigue strength.

All the Ti6Al4V specimens were manufactured by Beamit S.p.A. through an EOS M290 system equipped with a 400 W Yttrium fiber laser. The build chamber (sized 250x250x350 mm^2) was flooded with Argon to keep the Oxygen concentration below 0.1 %. The build platform was preheated up to 180 °C. The scan strategy was "stripes", rotated by 67° at each layer. The scanning order was to create the contour first, followed by the hatch scanning. The printing parameters are listed in Table 3. Before being removed from the platform, all the specimens underwent a solution annealing treatment to release the residual stresses consisting in heating up to 740 °C in a high vacuum furnace for a soaking time of 130 minutes. Annealing was followed by a controlled cooling phase down to 520 °C and successively quenching with Argon. All the fatigue-tested specimens were left in the as-built surface condition.

Table 2: Experimental campaign of Ti6Al4V alloy

Geometry	**Condition**	**Build orientation**	**Series ID**	**Number of specimens**
SEB (FCG)	Machined	Horizontal	Series H	15
		Vertical	Series V	15
Cylindrical (Axial Fatigue)	As-built	Vertical	Series VR	20
4PB (Bending Fatigue)	As-built	Horizontal	Series A	9
		45° (downskin)	Series D	16
		135° (upskin)	Series E	12

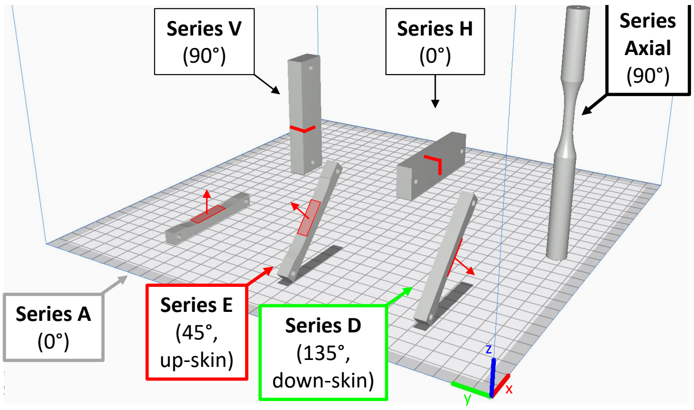

Figure 1: Layout of the L-PBF build plate indicating the specimen types and orientations with respect to the vertical direction (axis z).

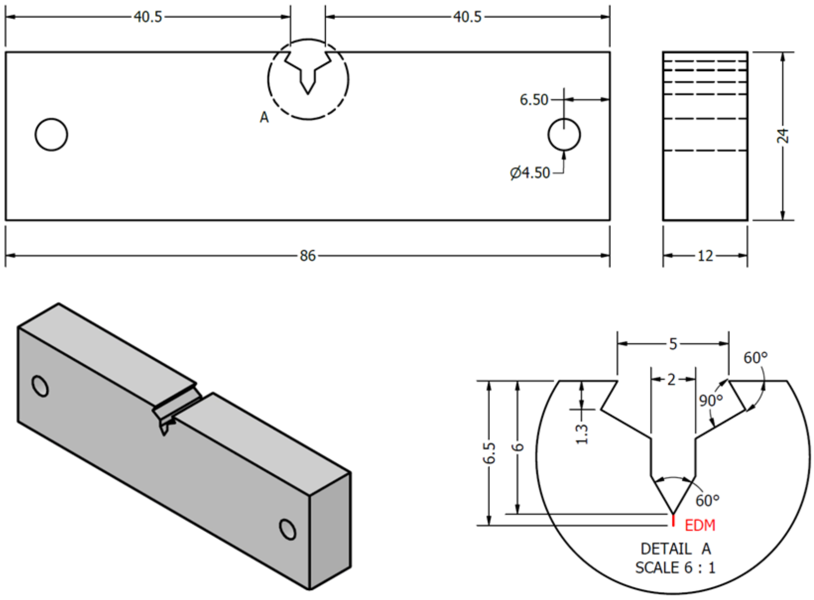

(a) SEB specimens for FCG tests

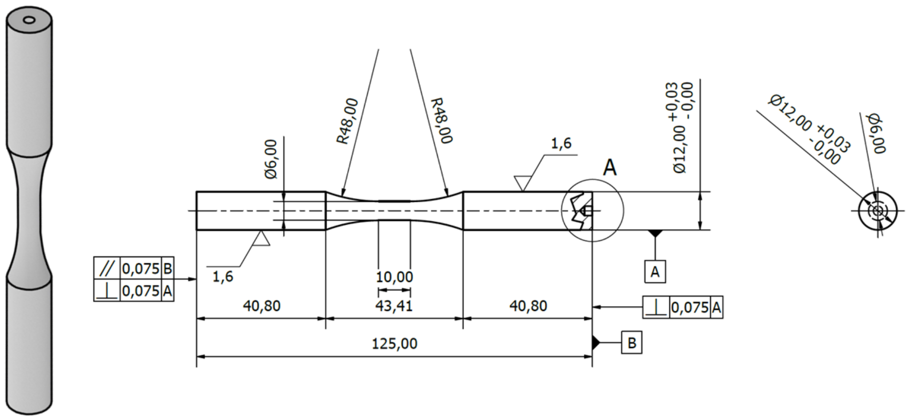

(b) Axial fatigue cylindrical specimens

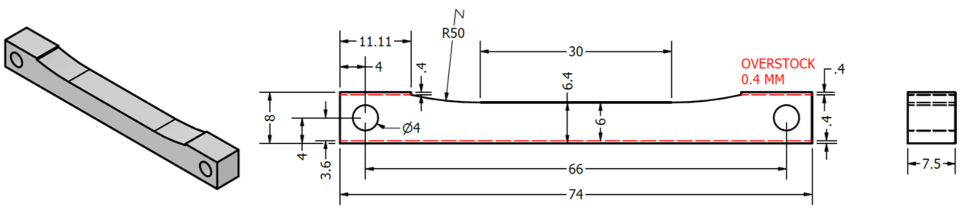

(c) 4PB fatigue specimens

Figure 2: Specimens geometries employed in the present study.

Table 3: Process parameters of EOS M290 L-PBF system.

Parameter	**Set point**
Laser Power [W]	340
Laser scan speed [mm/s]	1250
Layer thickness [μm]	60
Hatch distance [mm]	0.12
Laser Energy density [J/mm^3]	37.8

2.2. Microstructure

In this section, a hint is given on the morphology of the as-built surface and the underlying microstructure. It should be noted that the microstructure of the L-PBF Ti6Al4V alloy was already discussed in previous studies and the reader is also referred to them [19, 39–41].

A sample for each as-built series was cut along its longitudinal direction (cylinder axis for the axial vertical series, a direction perpendicular to the cross section and to the loaded surface for the 4PB series), embedded into an epoxy resin, polished and etched with Kroll's reagent. The etched sections were observed under a Zeiss AxioVision microscope at 10x magnification. The micrograph of each as-built series is shown in Figure 3. For all the build orientations, the typical microstructure of the annealed L-PBF Ti6Al4V parts is evident, with needle α' grains embedded in the prior columnar β grains elongated along the build direction (red arrow), still retained after the annealing treatment due to an incomplete martensite decomposition [42, 43]. The orientation of the prior β grains with respect to the loading direction strongly affects the anisotropy of the mechanical properties, while the presence of the martensitic phase increases the strength and, at the same time, limits the ductility of the alloy [43, 44].

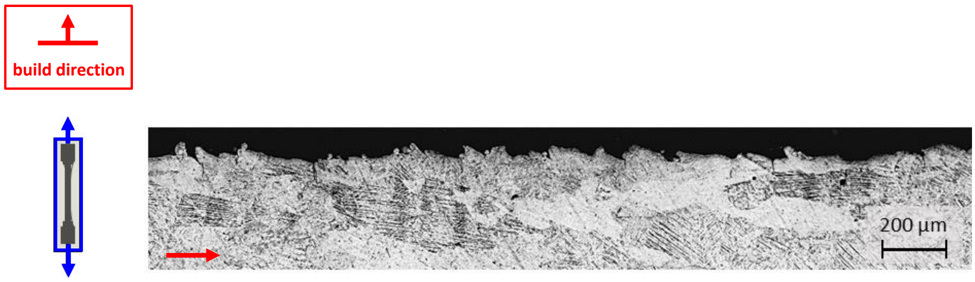

(a) Axial series Vertical

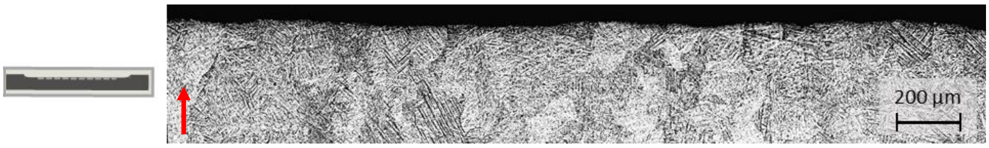

(b) 4PB series A (horizontal)

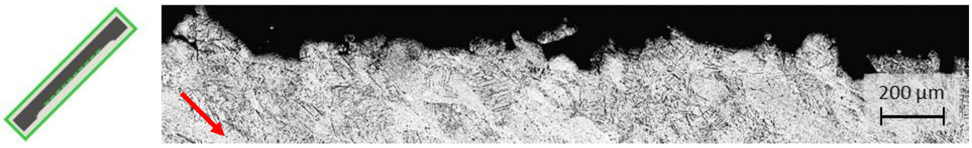

(c) 4PB series D (downskin)

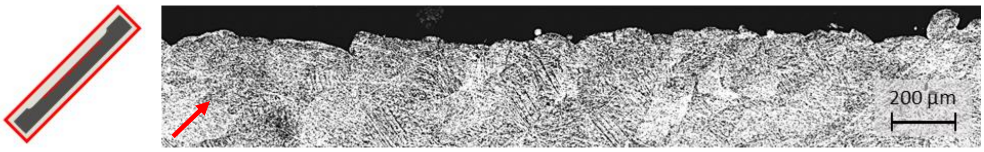

(d) 4PB series E (upskin)

Figure 3: Microstructure of the Ti6Al4V L-PBF alloy observed on etched polished sections of the specimens printed at different orientations. The red arrow indicates the build direction.

2.3. Tensile properties

The tensile tests were carried out employing 4 cylindrical samples tested under MTS RT100 tensiletest machine with a capacity of 100 kN. For tensile tests only, the specimens were machined reaching the following gauge dimensions: diameter $d_g = 6$ mm and length $l_g = 36$ mm.

The tensile properties of the Ti6Al4V alloy under investigation are summarized in Table 4. The table shows the mean values of the Ultimate Tensile Stress (UTS), the Yield Stress (S_y), the Elastic Modulus (E) and the Ultimate Tensile Strain (ϵ_U).

Table 4: Tensile properties of the Ti6Al4V alloy.

Property	**Mean**
UTS [MPa]	1127
Sy [MPa]	1089
E [MPa]	120432
ϵ_U [%]	14

2.4. Fatigue tests

Constant amplitude axial and bending fatigue tests were carried out at room temperature on a MTS servo-hydraulic machine with a loading frame having a capacity of 100kN. The testing frequency was chosen within the range $20 \div 40$ Hz according to the load level. All the fatigue tests were performed at the stress ratio R=0.1 and considering the failure condition as a stiffness drop of 10%. Specimens not failing after $5 \cdot 10^6$ cycles were considered as runouts and successively retested at higher stress levels up to failure to populate the S/N diagram in the finite life region. All the fracture surfaces were examined to determine the real cross section dimensions and calculate precisely the stress values.

2.5. Fatigue crack growth tests

Specimen precracking of SEB specimen was carried out in compression under an uniaxial Rumul Cracktronic resonant machine with load capacity of 100 kN. The specimens were subjected to cyclic bending with the aim of generating a plastic notch tip region in compression which then yields local tensile stresses when the external bending approaches zero. This procedure enables to nucleate a crack with limited load history effects [45].

After precracking, the FCG tests were performed according to the prescriptions contained in the standard ASTM E647 [46] and at 3 different stress ratios: R=-1, R=0.1 and R=0.7. Initially, all the specimens underwent a crack growth step under Constant Amplitude (CA) cyclic loading aimed to propagate and stabilize the crack front. Successively, depending on the target of the test, the second step can be performed i) considering a Load Reduction (LR) to measure the long crack threshold $\Delta K_{th,LC}$, or ii) proceeding with the CA to measure the crack growth rates in the Paris region. The crack advancement was monitored by means of a Rumul clip-on-gauge towards compliance measurements.

After testing, the SEB specimens were heat-tinted at 450 °C for 30 minutes and then statically broken under a three-point bending set-up after being soaked for 30 minutes in a bath of liquid nitrogen. Successively, the fracture surfaces were cleaned in ethanol by means of an ultrasonic cleaner. The fracture surfaces were observed under a Scanning Electron Microscope (SEM EVO 50, Zeiss) at different magnifications to spot the “killer defect” at the fracture origin.

2.6. Roughness measurements

The goals of the roughness measurements are the following:

- The calibration of the fatigue model is performed from known distribution of critical defect sizes measured from the tested specimens. In the present case of rough surface profiles, it is difficult to assess the defect depth as a clear reference of the ideal surface is missing from the fracture surfaces. Then, as it will be shown in the following, we propose to use the mean peak height $R_{p,m}$ to position the reference line on the fracture surface images and properly measure the size of the killer defect.
- Calculate an average geometric factor for each as-built series that takes into account the shielding phenomenon on the crack driving force (the stress intensity factor). In a previous work [35], we found that it is possible to estimate the average shielding effect on the crack SIF when multiple surface notches (with random morphology and distribution) are close to each other, averaging the roughness parameters calculated with the profile method. At this scope, we need to evaluate two average roughness parameters: the mean valley depth $R_{v,m}$ and the mean width of the profile elements R_{sm}.
- Together with a shielding factor, provide the roughness parameter maximum valley depth $R_{v,max}$ used for the fatigue life predictions. Successively, we will perform and compare the fatigue life predictions based on $R_{v,max}$ and those based on the average killer defect found on the fracture surfaces to assess the validity of adopting roughness-related parameters as equivalent initial defects for fatigue assessments of as-built parts.

The roughness measurements were performed on the specimens' surfaces at the side of the tensile stresses and were analysed according to the standard profile method. Three profiles for each specimen's surface were analysed along the longitudinal direction of the specimens (stress axis). The surface profiles were extracted from the topological reconstruction of the 3D surface under investigation. In detail:

- All the fatigue as-built series (1 specimen per series) were measured with *Alicona Infinite-Focus* FV (Focus-Variation) optical microscope. These acquisitions were carried out at a vertical resolution of 356 nm and a lateral resolution of 7.8 μm.
- Overhang 4PB series D and E (3 specimens per series) and axial vertical series (2 specimens) were also analysed by XCT to compare the two different measurement techniques.

XCT scans of series D and E specimens were carried out prior to testing on 3 specimens per series through a General Electric VTomex L 240kV XCT at Stellenbosch university facilities (South Africa). The settings used were 180 kV ands 80 μA for X-ray generation, 500 ms per image acquisition time, with 1600 images acquired in one full rotation of the sample. The voxel size was set at 15 μm. The XCT 3D specimen reconstruction of each specimen was handled with VGStudioMax 3.4.2. *(VolumeGraphics)*. The geometry was registered to a global Cartesian reference system and an ISO50 segmentation method [47] was applied for the surface determination. The segmentation consists in fixing a gray-intensity threshold to distinguish noise and material in the gray-intensity histogram of the XCT scan images, allowing to establish the boundary of the part within its environment (air). The resolution of the XCT was chosen to minimize the time and the effort for the scanning and for the data manipulation, according to what is prescribed by *du Plessis et al.* for roughness analyses from XCT-scanned surfaces [17], considering that a sub-voxel resolution for depth measurements can be reached by means of the segmentation [48].

In Matlab *(Mathworks)*, the primary profiles extracted from XCT and Alicona acquisitions were analysed to obtain the profile roughness parameters according to ISO 4287:1998 and ISO 4288:1998 standards [49, 50]. Each profile was extracted for a longitudinal length of 15 mm and was firstly denoised and then filtered with a Robust Gaussian filter with a cutoff wavelength λ_c=2.5 mm. This filtering process enabled to separate the contribution to the final profile of the long wavelengths, herein synthetically defined as waviness ($\overline{\lambda} > \lambda_c$), and the short wavelengths, or the roughness components ($\overline{\lambda} < \lambda_c$). The sampling length (i.e. length of a section i) for roughness measurements is equal to the filter cutoff wavelength $l_s = \lambda_c$=2.5 mm (Figure 4).

We calculate at each section i:

- the arithmetical mean of the ordinates (z_i) of the section i (roughness profile within a sampling length l_s):

$$R_{a,i} = \frac{1}{l_s} \int_0^{l_s} |z_i(x)| \, dx \tag{1}$$

- the max valley depth $R_{v,i}$ as the absolute value of the minimum (z_i) ordinate of the section:

$$R_{v,i} = abs(min(z_i)) \tag{2}$$

- the maximum peak height $R_{p,i}$ as the maximum (z_i) ordinate of the section:

$$R_{p,i} = max(z_i) \tag{3}$$

- the mean width of the profile features of the section $R_{sm,i}$: the calculation was performed according to the algorithm proposed by Scott [51, 52].

From the parameters calculated at each section i, average and maximum roughness parameters can be derived for the whole series (as average or maximum over all the sections of all the profiles of the series, see Figure 4).

The profile parameters (mean:R_a, $R_{v,m}$, R_{sm}, $R_{p,m}$; max: $R_{v,max}$, $R_{p,max}$) from the acquisitions with the FV optical microscope (Alicona) on all the as-built Ti6Al4V series are listed in Table 5, while the parameters referring to the XCT acquisitions of 4PB series D and E are listed in Table 6. Figure 5 shows the comparison between the FV optical microscope and XCT roughness parameters (average and standard deviation).

When performing the comparison between the two measurement methods, it is important to underline that the adopted lateral resolution of Alicona is smaller than the XCT voxel size, so we can take the FV optical measurements as reference to assess the quality of XCT measurements after the post-scanning steps and to perform the fatigue predictions.

XCT can provide reliable results for the depths measurement thanks to the fact that it allows a 3D reconstruction of the object scanned with X-rays. Its capability of spotting undercuts and re-entrant features of subsurface and surface anomalies, like sub-surface pore networks or deep open surface porosity [17, 22, 30, 32, 53, 54] gives the possibility to catch the surface shape with a good approximation. Moreover, a volumetric characterization of the surface defects distribution via XCT can be the starting point to build a fatigue life prediction model that considers the size and shape of surface anomalies, which have the maximum probability to act as crack initiation sites [55].

However, XCT technique often requires to make a trade-off between resolution and scan dimensions (only small portions of the object can be scanned at a high resolution due to physical constraints), other than being more expensive in terms of time and effort spent for scanning and data analysis [17, 53]. For the limitations in resolution of XCT, the optical methods can be useful for the surface characterization, despite the fact that there may be hidden valleys beneath protrusions or attached particles [30].

In the present case, the values of the valley depth and the peak height parameters are coherent between FV optical microscopy and XCT, both for the maximum $R_{v,max}$, $R_{p,max}$ and for the averaged $R_{v,m}$, $R_{p,m}$, thanks to the sub-voxel resolution for depth measurements on XCT surface. Therefore, our XCT measurements are accurate enough to obtain the parameters which are relevant to perform fatigue predictions. The values of $R_{v,max}$, $R_{p,max}$ are slightly, but systematically, larger with the XCT, because it can detect deeper and irregular depressions, while the optical method cannot pinpoint below the line of sight. Conversely, the chosen voxel size of the XCT does not allow to catch the smallest fluctuations of the profile (small valleys or protrusions of the surface) and this affects the R_a,$R_{v,m}$, $R_{p,m}$ that are seen to have slightly higher values respect to the optical method. Interestingly, also the spacing parameter R_{sm} is affected by the XCT voxel size. Indeed, the algorithm adopted for R_{sm} calculation [51, 52] applies vertical thresholds to determine which profile features are significant for the spacing. This implies that the resolution of the XCT measurements also affects the calculation of the shielding factor as the latter it directly related to R_{sm}.

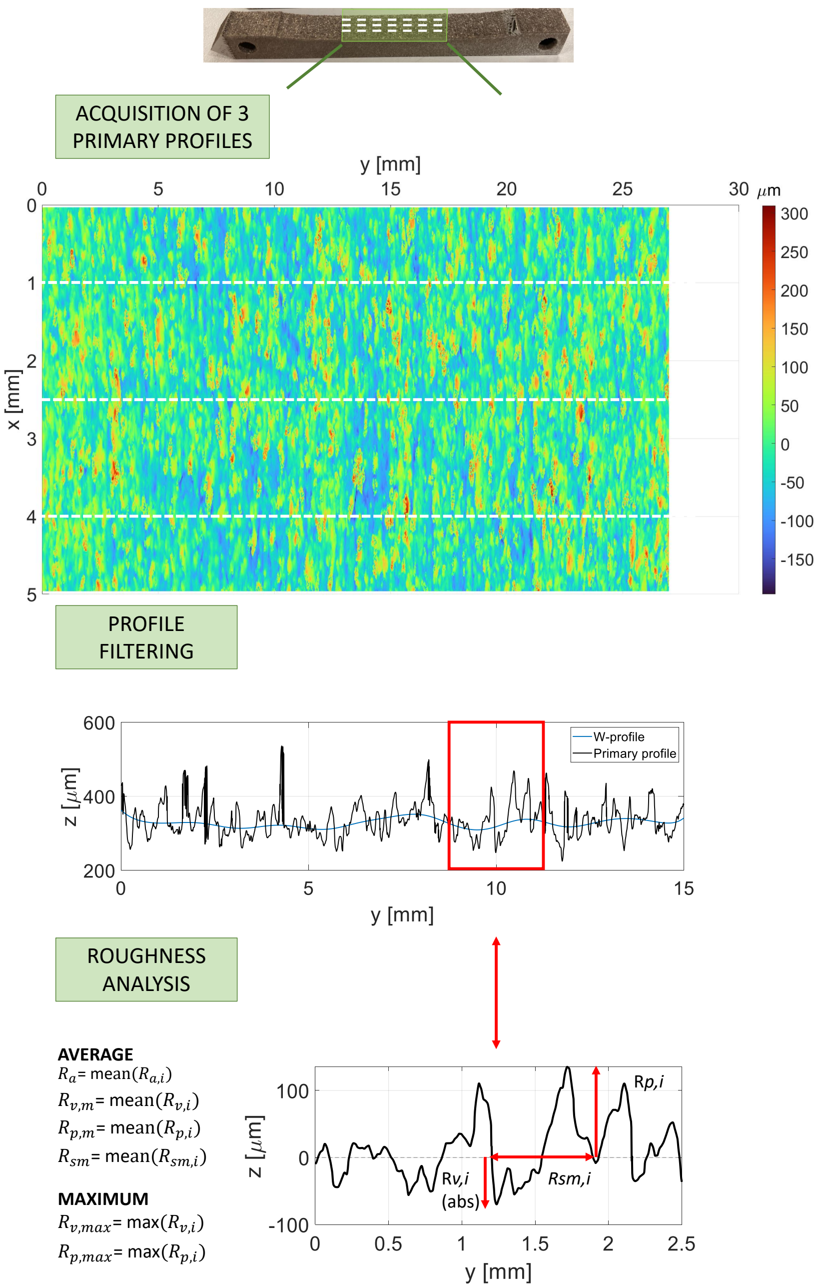

Figure 4: Roughness analysis with profile method from XCT for prediction purposes. The tested surface point cloud was exported from a XCT 3D reconstruction of the 4PB specimen. Three profiles per specimen were extracted and filtered. In detail, we are interested in the width X_i and depth $R_{v,i}$ of the profile feature in correspondence of the deepest valley for each section i.

Table 5: Main profile roughness parameters of the Ti6Al4V as-built series from FV optical microscope acquisitions.

Series	R_a [μm]		$R_{v,m}$ [μm]		R_{sm} [μm]		$R_{p,m}$ [μm]		$R_{v,max}$ [μm]	$R_{p,max}$ [μm]
	avg	std	avg	std	avg	std	avg	std		
Axial vertical	16	2	53	13	246	52	48	13	82	90
4PB - Series A	7	2	22	9	470	189	16	4	41	22
4PB - Series D	45	8	102	19	407	105	156	39	140	240
4PB - Series E	15	3	44	10	288	98	52	24	70	159

Table 6: Main profile roughness parameters of axial vertical series and 4PB series D and E from XCT acquisitions.

Series	R_a [μm]		$R_{v,m}$ [μm]		R_{sm} [μm]		$R_{p,m}$ [μm]		$R_{v,max}$ [μm]	$R_{p,max}$ [μm]
	avg	std	avg	std	avg	std	avg	std		
Axial vertical	12	2	34	11	326	58	39	11	54	78
4PB - Series D	30	7	69	22	281	98	142	50	152	272
4PB - Series E	13	2	41	19	367	132	50	25	104	132

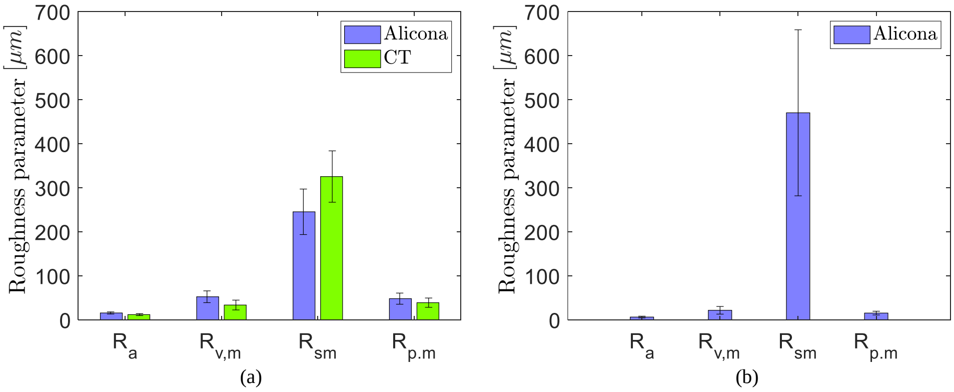

(a)

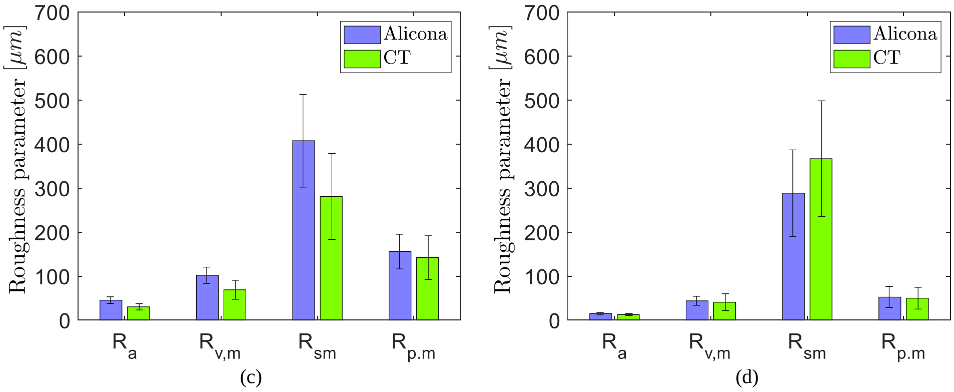

(b)

Figure 5: Average and standard deviation of the main profile roughness parameters adopted in this work. FV optical microscope (blue bars) measurements are compared to XCT ones (green bars): a) Axial series vertical, b) 4PB series A, c) 4PB series D, 4PB series E

3. Results

3.1. Fatigue tests

The S-N curves of the axial series is shown in Figure 6.a, whereas the S-N curves of the 4PB series A, D and E are presented in Figure 6.b. The scatter bands containing the 95% failure probability are displayed as shaded colored regions. The 50% regression curve (solid line) was obtained for each series by interpolating the experimental data-points in the finite life region with Equation 4 (standard ASTM E739 [56]):

$$N = A\Delta\sigma^{B} \tag{4}$$

The parameters A, B and the standard deviation σ_{logN} were derived from the regression with the maximum likelihood method and are listed in Table 7. Table 7 also contains the number of cycles to failure N_{lim} at the knee-point of the S-N curve and the experimental fatigue limit $\Delta\sigma_{w,exp}$, which is calculated as the average between the stress range at the last fatigue failure and the highest runout stress level.

The results show that the axial vertical and the downskin D series have the lowest fatigue limit among all the as-built fatigue series. Such series have a comparable fatigue limit, i.e. for vertical $\Delta\sigma_{w,exp} = 195$ MPa, for series D $\Delta\sigma_{w,exp} = 198$ MPa, but series D displays a larger scatter. The horizontal 4PB series A stands out for the best fatigue properties among the as-built series ($\Delta\sigma_{w,exp} = 428.5$ MPa). The upskin series E has a fatigue behaviour that is slightly higher than that of downskin series D in the endurance limit region ($\Delta\sigma_{w,exp} = 221$ MPa), while in the finite life region, despite the quite large scatter shown by both series, the data are overlapped.

Table 7: Parameters of the S-N curves of the Ti6Al4V as-built series

Series	$\Delta\sigma_{w,exp}$ **[MPa]**	N_{lim} **[cycles]**	σ_{logN}	**A**	**B**
Axial (R=0.1)	195	650990	0.091	$1.54 \cdot 10^5$	4.318
4PB (R=0.1) - A	429	273756	0.079	$1.39 \cdot 10^5$	4.146
4PB (R=0.1) - D	198	552000	0.163	$1.72 \cdot 10^5$	3.582
4PB (R=0.1) - E	221	574260	0.191	$2.12 \cdot 10^5$	4.125

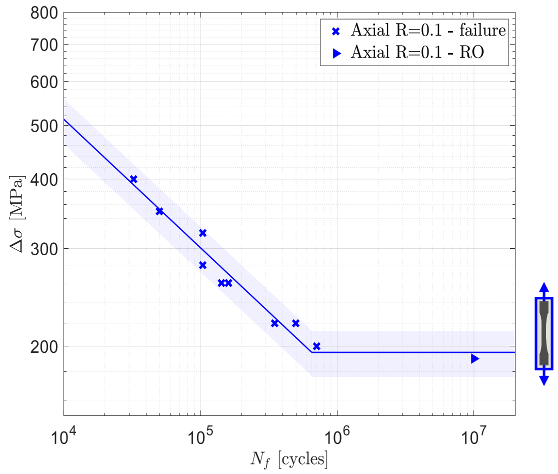

(a)

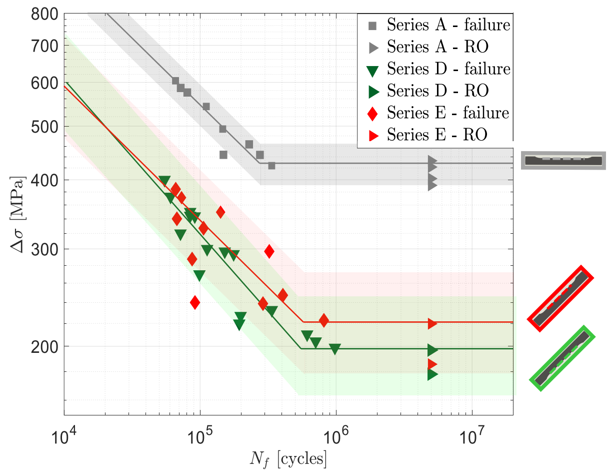

(b)

Figure 6: S-N of Ti6Al4V alloy: a) Axial fatigue vertical series; b) 4PB series.

The critical features observed from the fracture surfaces of the fatigue specimens are reported in Figure 7. No internal porosity or Lack of Fusion (LOF) defects were found on the observed fracture surfaces. Some of the axial fatigue vertical as-built cylindrical specimens displayed a single crack initiation site on the outer surface, as shown in Figure 7.a, others were characterised by multiple initiation sites on the surface successively leading to a single dominant crack front.

For the 4PB horizontal series A, the crack leading to failure started from either a single or multiple crack initiation sites on the loaded surface, in correspondence of small triangular-shaped surface defects. These defects are the projections on the fracture surface plane of the intersections between the welded tracks that correspond to the “primary roughness” [23] due to the solidification of the melt pool and to the remelting of the top horizontal surface of these specimens. Fatigue specimens with a similar surface condition were tested by other authors [11, 34, 38, 40].

The fatigue failure of overhang 4PB series D and E always initiated from the grooves of the rough loaded surface, usually from multiple initiation sites. Some tear ridges and different planes of crack propagation were found on the fracture surfaces. The loaded surface of Series D is a downskin surface, which is highly rough, due to the deep surface valleys and the presence of spatter and partially melted or unmelted particles attached onto it. These features are visible on the fracture surfaces observed through SEM (Figure 7.c).

Series E (Figure 7.d) is characterised by an upskin loaded surface that is smoother than that of series D but rougher than that of the horizontal series A. This surface is characterised by a pronounced waviness shaped by the laser scan tracks (much more pronounced with respect to the tracks retained on the horizontal top surface of series A) and by the stratification of layers during printing (stair-case effect); it also presents partially melted or unmelted particles attached onto it.

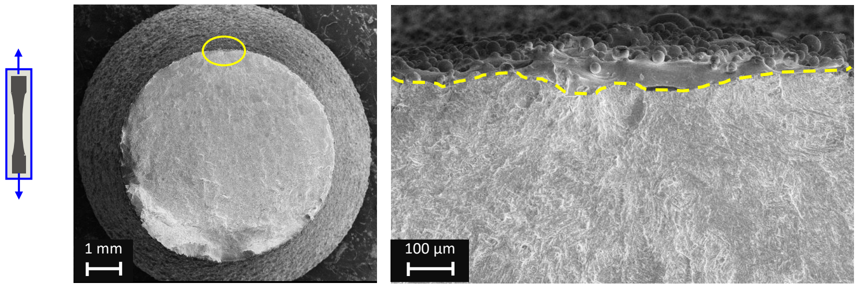

(a) Axial fatigue cylindrical specimens

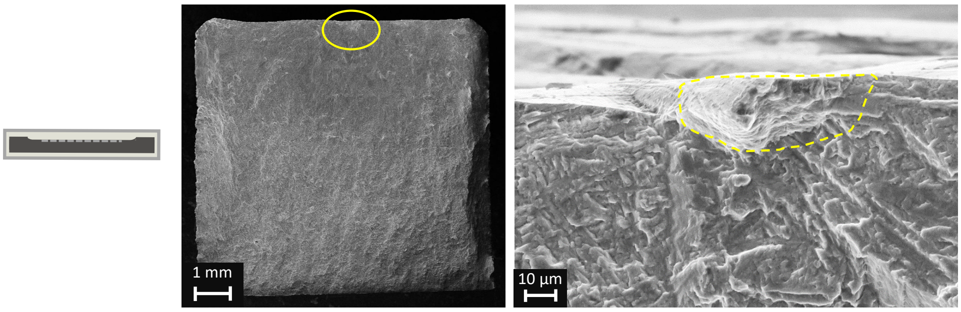

(b) 4PB series A (horizontal)

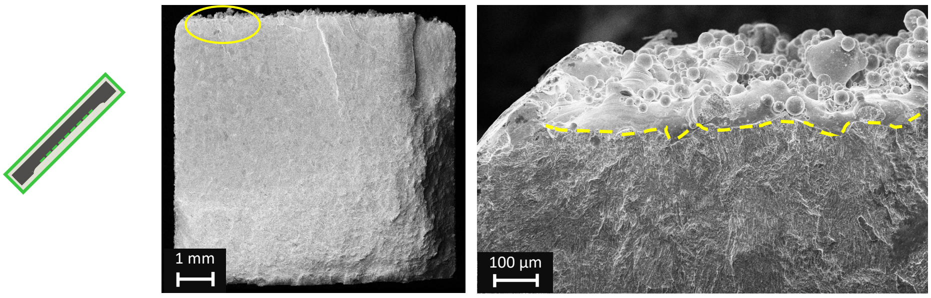

(c) 4PB series D (downskin)

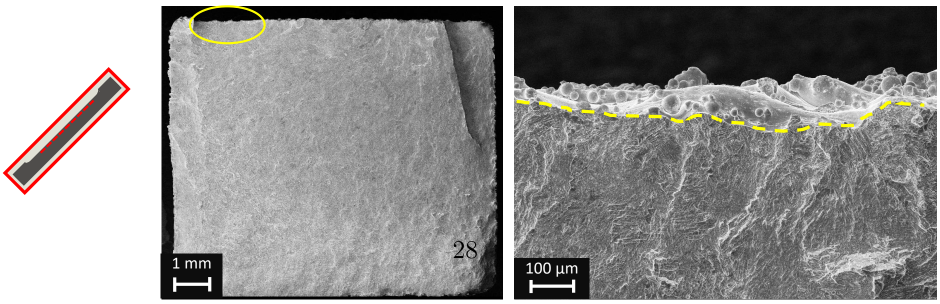

(d) 4PB series E (upskin)

Figure 7: Type of defects from fractography of Ti6Al4V L-PBF specimens.

3.2. FCG results

The long crack thresholds $\Delta K_{th,LC}$ and the crack growth rate data are reported in Figure 8.a-b. It is interesting to notice that the crack growth properties of the present Ti6Al4V alloy do not depend upon the specimen orientation for positive load ratios, while they display slightly different values for negative load ratio. In particular, for $R = -1$, we observed a lower $\Delta K_{th,LC}$ for the specimens manufactured vertically indicating that a crack plane parallel to the building plane is more favorable for crack propagation.

A similar lack of anisotropy of the threshold range $\Delta K_{th,LC}$ at positive load ratios was found by Leuders et al. [57] and by Hasib et al. [58] in the as-built state (no heat treatments) or with heat treatments at temperatures that guarantee a similar grain size with respect to the one found in as-built specimens. For both authors, the average $\Delta K_{th,LC}$ at the stress ratio R=0.1 of the material heat-treated below the β-transus temperature is close to 4 $MPa\sqrt{m}$, which is a value also found for conventionally manufactured materials [59] and close to the value measured in the present study (3.5 $MPa\sqrt{m}$). We note that heat treatments applied at higher temperatures and/or for a longer holding time have the double effect of releasing the internal stresses [57] and of coarsening the microstructure [58] imparting differences in the FCG resistance with respect to the as-built condition.

The experimental $\Delta K_{th,LC}$ data (Table 8) were used to fit the NASGRO 4.0 equations for thresholds:

$$\Delta K_{th} = \Delta K_1^* \frac{\left[\frac{1-R}{1-f}\right]^{(1+RC_{th}^p)}}{(1-A_0)^{(1-R)C_{th}^p}} \quad for\, R \geq 0, \quad where \quad f = max(R, A_0 + A_1 R + A_2 R^2 + A_3 R^3);$$
$$\Delta K_{th} = \Delta K_1^* \frac{\left[\frac{1-R}{1-f}\right]^{(1+RC_{th}^m)}}{(1-A_0)^{(C_{th}^p - RC_{th}^m)}} \quad for\, R < 0, \quad where \quad f = A_0 + A_1 R. \tag{5}$$

with

$$\Delta K_1^* = \Delta K_1 \sqrt{\frac{a}{a+a_0}} = \Delta K_1 \tag{6}$$

As a matter of fitting the Equations 5 and 6, we can consider that during the FCG tests the crack length a is much longer than the short crack parameter a_0 and then $\frac{a}{a+a_0} \rightarrow 1$. This assumption will be released when the Equations 5 and 6 will be used to perform the fatigue life calculations, a proper short crack parameter a_0 will be considered. The term f is the Newman's closure function that describes the crack closure effect in function of the stress ratio R. The parameters $A_{0,1,2,3}$ are derived by:

$$
\begin{aligned}
A_0 &= \left(0.825 - 0.34\alpha + 0.05\alpha^2\right)\left(cos\left(\frac{1}{2}\frac{\sigma_{max}}{\sigma_0}\right)\right)^{1/\alpha} \\
A_1 &= (0.415 - 0.071\alpha)\,\frac{\sigma_{max}}{\sigma_0} \\
A_3 &= 2A_0 + A_1 - 1 \\
A_2 &= 1 - A_0 - A_1 - A_3
\end{aligned}
\tag{7}
$$

with $\alpha = 2$ (constraint factor) and $\frac{\sigma_{max}}{\sigma_0} = 0.3$ (maximum stress/flow stress). The flow stress for the present material is set to $\sigma_0 = \frac{UTS+S_y}{2} = 1108$ MPa. The $\Delta K_{th,LC}$ - R fitting curves are shown in Figure 8.a, while the experimental values and the values obtained with the fitted NASGRO equation are given in Table 8.

Table 8: Experimental vs NASGRO threshold range $\Delta K_{th,LC}$ for horizontal and vertical build orientations at the stress ratios: R=-1, R=0.1, R=0.7.

Series/$\Delta K_{th,LC}$ $[MPa\sqrt{m}]$	R=-1		R=0.1		R=0.7	
	Exp.	Nasgro	Exp.	Nasgro	Exp.	Nasgro
V	6.08 6.08	6.08	3.64 3.26	3.44	2.04	2.04
H	6.77 6.63	6.7	3.44	3.45	2	2

The crack growth rate data were used to fit the NASGRO equation:

$$
\frac{da}{dN} = C\left[\left(\frac{1-f}{1-R}\right)\Delta K\right]^m \frac{\left(1 - \frac{\Delta K_{th}}{\Delta K}\right)^p}{\left(1 - \frac{K_{max}}{K_c}\right)^q}
\tag{8}
$$

The fitting parameters C, m, and p for the FCG curves in the two orientations (vertical and horizontal) are listed in Table 9. The parameter q, which describes the condition of unstable crack propagation (that occurs when the maximum SIF K_{max} reaches the fracture toughness K_c) is set to zero. The NASGRO equation can model precisely the crack growth rates for the load ratio $R = 0.7$ and $R = -1$. In fact, the crack growth rate data for these two load ratio, in the Paris region, follow the same linear trend in log-log scale. The load ratio $R = 0.1$ is characterised by a slightly higher slope, however the fitting was forced to follow the other two load ratios and for this reason we consider this choice the most suited for representing the present experimental data. However, we note that the fit of the $R = 0.1$ data is still consistent with the analytical equation for crack growth rates lower than 10^{-9}m/cycle in the threshold region. The lack of anisotropy between horizontal and vertical build orientations at positive R ratios is also evident in the Paris region Figure 8.b of the FCG curves, confirming the evidence found by other authors for both the as-built [60] and the heat-treated conditions [61, 62].

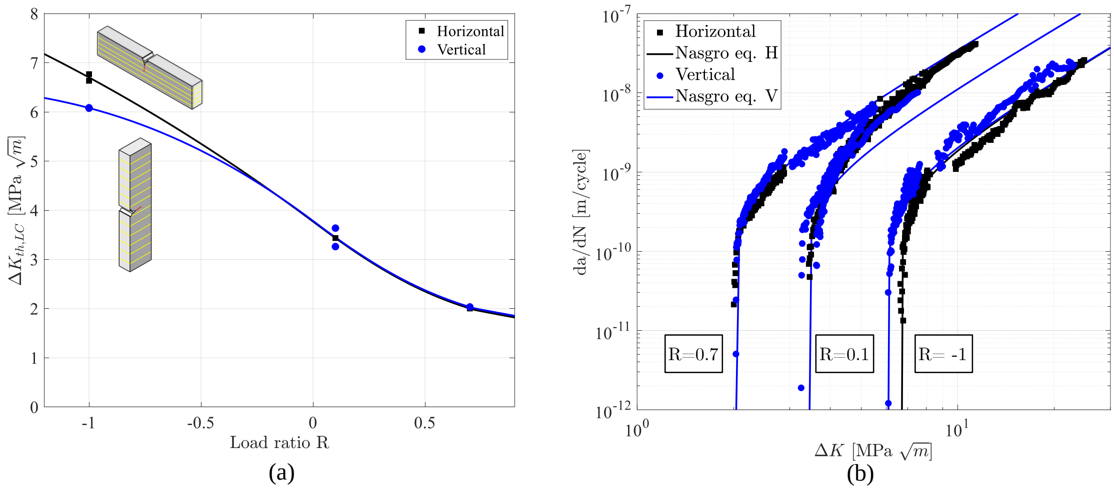

Figure 8: NASGRO fitting curves: a) Long crack thresholds vs load ratio R; b) FCG curves.

Table 9: Fitting parameters of NASGRO equation for long crack thresholds and FCG curves for horizontal and vertical build orientations. Values of the parameters consider ΔK in $[MPa\sqrt{m}]$ and crack growth rate da/dN in $[m/cycle]$

Series	ΔK_I $[MPa\sqrt{m}]$	C_{th}^p	C_{th}^m	**C**	**m**	**p**
V	1.66	1.08	0.17	$2.8 \cdot 10^{-10}$	2.34	0.5
H	1.63	1.13	$6.31 \cdot 10^{-4}$			

4. Analysis of critical defects

4.1. Definition of critical defect size

A fatigue assessment based on the fracture mechanics theory requires the specification of an initial equivalent defect size. The size of the defects found at the fracture origin of the investigated specimens (Figure 7) is herein associated to the Murakami's parameter $\sqrt{area}$. According to the Murakami's theory [63], the fatigue limit of defective materials, or materials having surface micro-notches, can be analyzed according the fracture mechanics theory. The crack driving force expressed as the SIF in mode I of the defects/micro-notches can be simply written as:

$$K_I = Y\,\sigma_0\,\sqrt{\pi\,\sqrt{area}} \tag{9}$$

where Y is the Murakami's boundary correction factor (Y=0.5 for internal defects, Y=0.65 for surface defects), $\Delta\sigma_0$ is the remote applied stress and $\sqrt{area}$ is:

- the square root of the area of the single 3D defect projected on a plane perpendicular to the loading direction if the defect is internal, sub-superficial or superficial and has an aspect ratio $w/t < 10$ (w=defect width, t=defect depth). For these cases, $\sqrt{area}$ is derived from the area of the smooth envelope of the feature at the fracture origin that is observed from the fracture surfaces;
- the quantity $\sqrt{10} \cdot t$ for a shallow defect that has an aspect ratio $w/t \geq 10$. If the failure started from a valley of a rough surface (case of 4PB as-built overhang series D and E) it is equal to the quantity $\sqrt{10} \cdot t_{max}$ where t_{max} is the maximum groove depth.

In general, the killer defect's size measurement method is straightforward for internal and sub-surface defects. However, such defect types are not relevant in our specific case because only few sub-surface defects were observed that did not contribute to the fatigue failure. On the other hand, the determination of the equivalent killer defect size for superficial defects correlated with AM rough surfaces requires further considerations as there are no clear guidelines in literature. One possibility is to consider the crack depth as the whole height of what is detectable on the fracture plane, that is embedding the protrusions (spatter, metal tracks, attached particles) into the defect size. This approach would lead to overestimating the defect size due to the fact that the surface protrusions do not carry stress. Another option is to define a proper reference line from which the defect sizes can be calculated.

In this work, we are proposing two strategies to position a reference line for the measurements of the surface features on the fracture surface images. The first method, i.e. what we consider

the most accurate, is to analyze the XCT 3D reconstruction of the loaded surface. We performed this kind of analysis after extracting the data point of the surfaces of interest from the 3D reconstructed geometry obtained from XCT scanning series D and E specimens (3 per series) prior to testing. In particular, in VGStudioMax 3.4.2, after the registration and segmentation steps, and once the specimen's boundary is determined, a ROI (Region Of Interest) can be created by means of a clipping box that selects only a portion of the loaded surface within the gauge length. The geometry included in the ROI can be exported as a 3D mesh or point cloud. The point cloud was successively imported into the Matlab environment and the surface points were fitted with a Least Squares plane that is the reference for depth measurements. A 3D grid-interpolation of the surface points was performed at a resolution of 5 μm to obtain a continuous surface mesh.
After the 4PB fatigue test, and before breaking the 4PB specimens in brittle mode, the distance h of the specimens' fracture surface position with respect to the mid-section was measured by image analysis (Figure 9a).

The measurements performed on the post-failure specimens were used to spot the surface features on the before-testing XCT reconstructed geometry. The fracture surface position was identified on the 3D surface in Matlab and the surface map, e.g. the one in Figure 9.a, was analyzed visually. Figure 9.a only shows the valleys of the 3D surface of a specimen of series D, because the protrusions are hidden behind the black least squares (LS) fitting plane: this kind of visualization and the valleys color scale (from green to blue) helps identifying the deepest valleys (blue colored areas) close to the fracture surface position (that we call *critical valleys*).

After localising the critical valleys, the 3D surface was re-scaled by subtracting the LS fitting plane from the surface heights, so that the reference plane for height measurements becomes the x-y plane of the global reference system (e.g. Fig. 9.b). The fracture origin position on the SEM fractography images was identified and re-scaled to the reference system adopted for the 3D surface in Matlab, so that the x coordinate of the defect position could be compared. A reference line was drawn on the fracture surface image (white solid line in Figure 9.c), starting from the deepest valley at the fracture origin and going upwards of an amount equal to the critical valley's depth detected in Matlab. In this way, we found the position of the LS fitting plane projection on the SEM image. The highest peaks surrounding the critical valley were also identified in Matlab and their height was compared with the size of the protrusions found on the fracture surface images at the corresponding positions. The peak heights and the valley depths of the XCT scanned surface were in agreement with the fractography observations.

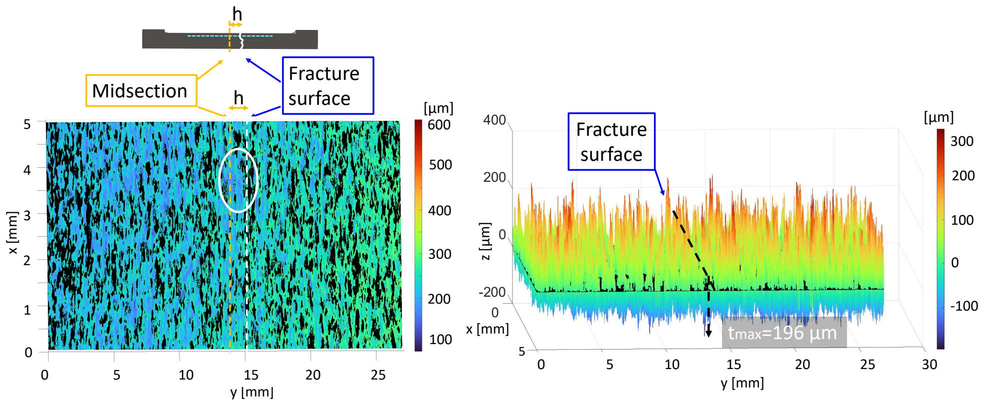

(a)

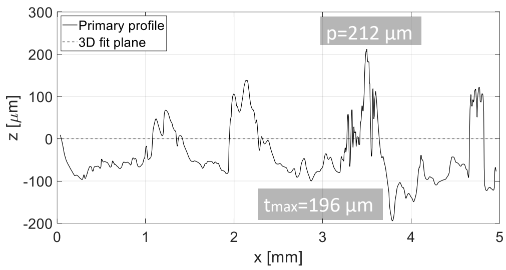

(b)

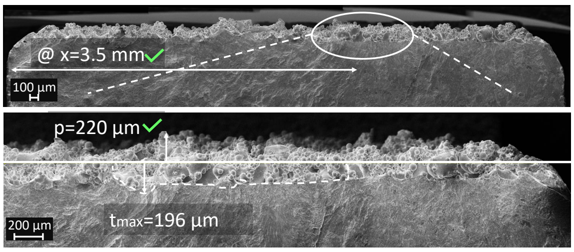

(c)

Figure 9: Mean plane determination from XCT: a) The fracture plane location on the surface map is determined starting from the distance h from the midsection. The critical valley's coordinates are identified. b) The critical valley depth and the height of the protrusions close-by are taken with respect to the LS plane; c) The reference line (projection of the LS plane) is positioned on the SEM image starting from the deepest valley and going up of an amount equal to the critical valley depth measured on the XCT surface map. The maximum protrusion close to the deepest valley has the same height of the peak measured on the surface map.

An alternative method to position the reference line is based on the profile roughness. After positioning the LS fitting plane on the fracture surface images of the 6 specimens that were analysed by XCT scans, we used average roughness parameters to obtain an approximate position to the reference line. The method consists of:

- identifying the frontal surface features at the crack initiation zone on fractography images (paying attention to not consider the features that are in the rear of the fracture plane);
- positioning the reference line starting from the highest frontal protrusion and moving downwards of an amount equal to the mean peak height $R_{p,m}$ obtained from profile roughness measurements;
- considering as killer defect only the groove region that is beneath the reference line.

The aim of this second method is to understand if we can use solely profile roughness parameters without resorting to the XCT technique. In the following, we compare the three methods for the defect size measurements as illustrated in Figure 10.a:

- Total height: considering the envelope of all the surface features at the crack initiation zone;
- XCT: positioning the reference line through the projection of the LS-fitting plane of the XCT 3D reconstruction of the whole surface;
- Approximate: positioning the reference line through the average roughness parameter $R_{p,m}$.

The comparison of the 3 methods applied on the specimens of series D and E that were XCT-scanned before the fatigue test is illustrated in Figure 10b-c and in Table 10.

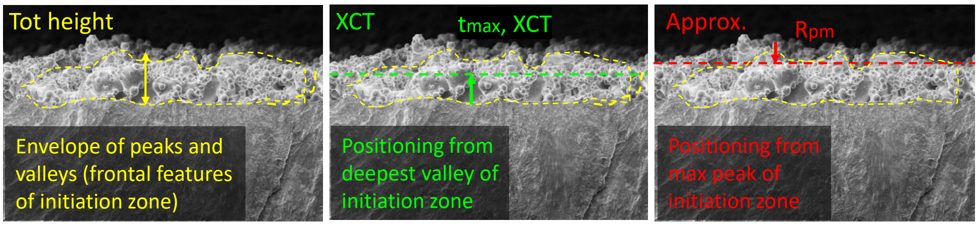

(a)

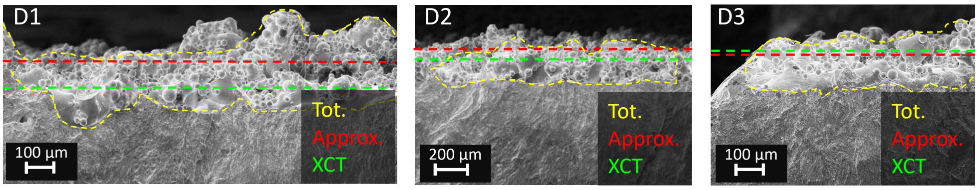

(b)

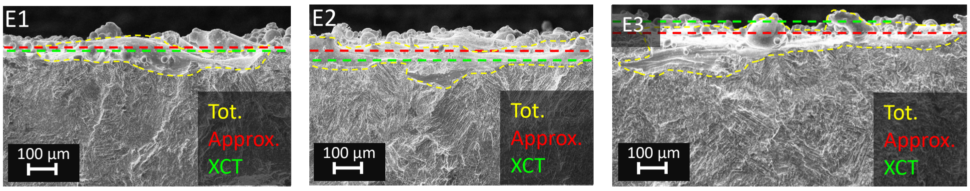

(c)

Figure 10: Three methods for the defect size measurements: a)Total height vs XCT reference line vs Approximate reference line methods on a specimen of series D; b)comparison on series D specimens; c)comparison on series E specimens.

Table 10: Comparison of the equivalent crack size obtained from the three different measurement methods on the XCT-scanned specimens of series D and E (3 specimens per series)

Series	**Specimen id**	**Method**	**Height** **t** $[\mu m]$	**Width** **w** $[\mu m]$	$\sqrt{area}$ $[\mu m]$
4PB -Series D	1	XCT	160	1860	506
		Approx.	262	1860	534
		Tot height	424	1860	716
	2	XCT	196	1760	555.3
		Approx.	226	1760	613.6
		Tot height	383	1760	670
	3	XCT	180	1800	569
		Approx.	172	1800	544
		Tot height	290	1800	660
4PB -Series E	1	XCT	75	1070	237.2
		Approx.	88	1070	278.3
		Tot height	140	1070	309.2
	2	XCT	80	1075	253
		Approx.	123	1075	245
		Tot height	180	1075	301
	3	XCT	190	1490	366
		Approx.	141	1490	446
		Tot height	192	1490	353

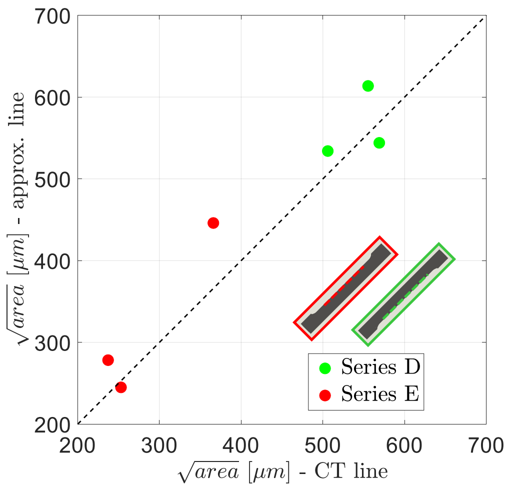

Figure 11: Comparison of $\sqrt{area}$ parameter measured on fracture surfaces with the adoption of XCT and the Approx. reference lines.

From Figures 10 and Table 10, it is evident that the total height method provides larger defect sizes compared to the other two methods that involve a reference line. Conversely, the adoption of the approximate reference line rather than the more accurate method based on XCT provides a fair agreement in the defects' depth measurements. Figure 11 compares the $\sqrt{area}$ parameter measured on fracture surfaces with the adoption of XCT and the approximate reference lines.

The horizontal line cuts the defect's envelope, excluding the highest protrusions that can be observed on the fracture plane, thus reducing the defect's depth. It is worth underlining that the defect's aspect ratio also changes considering the reference line method. In general, the defect's width remains the same, while its depth decreases. The consequence is that all the defects measured with the reference line tends to be elongated, i.e. tend to have an aspect ratio $w/t \geq 10$. Once the shape of the defect is fixed as elongated, the defect's size only depends on the maximum groove depth detected on the fracture surface. This consideration is not valid for the total height method that suffers from the variability introduced by the defect's aspect ratio.

4.2. Distribution of critical defects

The maximum defect $\sqrt{area}$ data for each series were interpolated by a LEVD, whose cumulative density function is given by:

$$F_{LEVD} = exp\left[-exp\left(-\frac{x-\lambda}{\delta}\right)\right] \tag{10}$$

x is the max $\sqrt{area}$ for each specimen, λ and δ are the location and the scale parameters, respectively, which were derived from the regression with the Maximum Likelihood method.

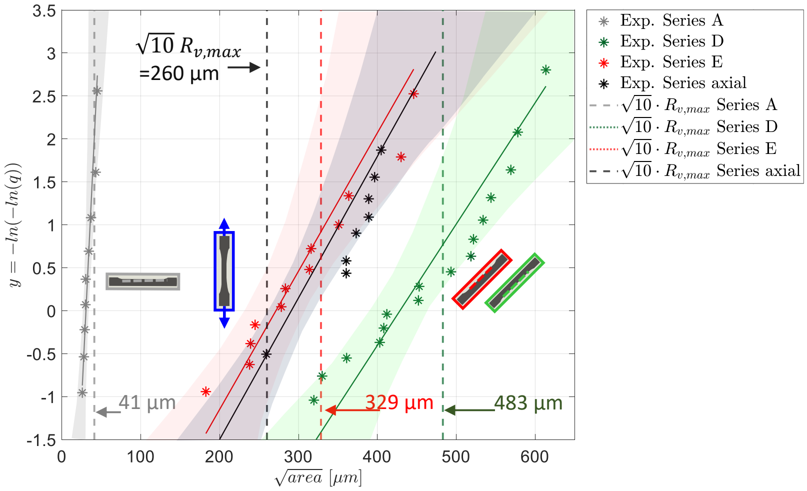

Figure 12: LEVD of maximum defect size in terms of $\sqrt{area}$ of the Ti6Al4V as-built series (measured with approximated reference line method). A vertical dashed line is plotted for each series, representing the $\sqrt{10} \cdot R_{v,max}$ from the profile roughness measurements of the series.

The probability plot showing the data of the 4PB series A (grey stars), D (green stars) and E (red stars) and of the axial series (black stars) are displayed in Figure 12. Considering that i) the XCT scans were not performed for all the specimens and ii) the approximate reference line method yields robust results (Figure 11), the $\sqrt{area}$ of the data-points for the rough series were all calculated with respect to the approximate reference line. The LEVD regression line is represented by a solid line, while the shaded colored area is the region included in the bilateral 95% confidence bands. An additional dashed vertical line is plotted in Figure 12 for each series (same color code of LEVD distributions) to represent the value of the equivalent 2D crack size $\sqrt{10} \cdot R_{v,max}$ as obtained from the maximum valley depth retrieved from the profile roughness measurements of the series.

Table 11: Main parameters of the distribution of killer defect size (max $\sqrt{area}$) of the Ti6Al4V as-built series measured with the approximate reference line method on the fracture surfaces (LEVD fitting parameters, average aspect ratio and $\sqrt{area}_{50\%}$ parameter). For sake of comparison, the values of the $\sqrt{10} \cdot R_{v,max}$ parameter from profile roughness are listed for all the series.

Series	$\lambda\,[\mu m]$	δ	$\sqrt{area}_{50\%}\,[\mu m]$	$\sqrt{10}\,R_{v,max}\,[\mu m]$	$(c/a)_{avg,in}$
Axial vertical	291	61	362	260	6.9
4PB - Series A	31	5	33	41	1.8
4PB - Series D	429	71	437	483	4.1
4PB - Series E	271	62	294	329	5

A summary of the LEVD parameters is reported in Table 11. Considering the values reported in the Table, some observations are summarized in the following:

- The Table 11 includes the LEVD fitted parameters λ and δ, the scale parameter δ determines the slope of the regression line, while λ its position on the probability plot.
- The average aspect ratio of the killer defects observed on the fractography images $(c/a)_{avg,in}$ (initial crack aspect ratio) is calculated considering the initial crack depth a taken as the average depth and the initial crack width c taken as the average semi-width $c = w/2$.
- The $\sqrt{area}_{50\%}$ corresponds to the $\sqrt{area}$ at the 50% probability obtained from the LEVD distributions, calculated as [64]:

$$\sqrt{area}_{50\%} = \lambda - \delta \cdot log(-log(0.5)) \tag{11}$$

- The $\sqrt{10} \cdot R_{v,max}$ corresponds to the max valley depth from profile roughness parameters. For series D and E for which XCT scans are available, $R_{v,max}$ is calculated from profiles extracted from the XCT reconstructed surfaces, while for the other series it is taken from Alicona measurements.

The fact that the 4PB series D has the lowest slope among the series, and that is shifted on the right, indicates that it is likely to have a large surface feature (surface groove) at the fracture origin. Oppositely, series A has the highest slope and is shifted on the left, indicating that the fatigue failure is more likely to start from small-sized surface micro-notches than from a deep surface groove. The vertical axial series has intermediate defect sizes between the horizontal (best surface quality) and the downskin ones (worst surface quality).

5. Fatigue model

5.1. Threshold model

A fracture mechanics-based fatigue model requires to properly consider the short-crack effect as it influences particularly the predictions in the endurance limit region. To account for the short-crack effect, we adopted the El-Haddad equation [65] which expresses the fatigue limit range $\Delta\sigma_w$ as a function of the Murakami's equivalent crack size $\sqrt{area}$:

$$\Delta\sigma_w = \Delta\sigma_{w,0}\sqrt{\frac{\sqrt{area_0}}{\sqrt{area}+\sqrt{area_0}}} \tag{12}$$

Equation 12 can be also expressed in terms of SIF:

$$\Delta K_{th} = \Delta K_{th,LC}\sqrt{\frac{\sqrt{area}}{\sqrt{area}+\sqrt{area_0}}} \tag{13}$$

In both equations 12 and 13, the El-Haddad parameter is defined as:

$$\sqrt{area_0} = \frac{1}{\pi}\left(\frac{\Delta K_{th,LC}}{Y\cdot\Delta\sigma_{w,0}}\right)^2 \tag{14}$$

where

- $\Delta K_{th,LC}$ is the long crack threshold at the stress ratio R of interest, obtained from the NASGRO equation (Equation 5) fitting for the two orientations (horizontal and vertical);
- $\Delta\sigma_{w,0}$ is the theoretical endurance limit range of the defectless Ti6Al4V alloy, which was determined from the Goodman model on the Haigh diagram at the stress ratio R of interest (starting from the value of $\Delta\sigma_{w,0}$ at R=-1: $\Delta\sigma_{w,0,R=-1} = 2\cdot(0.5\cdot UTS)$= 1127 MPa);
- Y=0.65 is the geometric factor for surface defects when Murakami's SIF expression is adopted.

5.2. Shielding effect

Murakami's theoretical model for the shielding factor, which was found empirically for regular artificial surfaces, was adapted to as-built L-PBF surfaces by Barricelli and Beretta [35]. They found that averaged R_v and R_{sm} parameters allow to calculate an average geometric factor $\overline{F}$ that globally describes the shielding effect of the interacting cracks at the valleys of a rough surface with random morphology.

Setting $a = R_{v,m}$ and $b = R_{sm}$ in Equations 15 [24]:

$$\begin{aligned} \frac{\sqrt{area_R}}{b} &\cong 0.97\left(\frac{a}{b}\right) - 3.51\left(\frac{a}{b}\right)^2 - 9.74\left(\frac{a}{b}\right)^3 \quad \text{for } 0 < \frac{a}{b} < 0.195; \\ \frac{\sqrt{area_R}}{b} &\cong 0.38 \quad \text{for } 0.195 < \frac{a}{b} < 3 \end{aligned} \tag{15}$$

and calculating the average geometric factor as (Equation 16)

$$\overline{F} = 0.65\sqrt{\frac{\sqrt{area_R}}{a}} \tag{16}$$

the average shielding factor $\overline{F}$ for each as-built series yields the values listed in Table 12.

Table 12: Average shielding factor $\overline{F}$ from standard roughness parameters of Ti6Al4V as-built series

Series	$\overline{F}$
Axial vertical (together)	0.9
4PB - Series A	1.12 (unshielded)
4PB - Series D	0.8
4PB - Series E	1

Series A is unshielded because the horizontal build orientation guarantees that the tested surface is smooth enough not have any interaction effects between the surface notches. Its average geometric factor is 1.12 that is the geometric factor of a single edge crack in a semi-infinite plate (SIF expression: $K_I = 1.12\sigma\sqrt{\pi\, a}$ with a=crack depth), which is indeed the condition of "isolated" crack (single 2D edge crack in a semi-infinite plate).

The lower the value of $\overline{F}$ with respect to the max value 1.12, the more shielded is the crack at the root of the killer defect, due to the interaction with cracks close-by that reduce its SIF. Series D is the most "shielded" series.

5.3. Endurance limit prediction

In this section, the experimental fatigue data are plotted on the Kitagawa-Takahashi diagram and compared to the El-Haddad model. Figure 13 shows the comparison between the experimental fatigue data (SIF range vs $\sqrt{area}$) of the 4PB series D and the El-Haddad model in terms of SIF range for the vertical threshold $\Delta K_{th,LC}$ (black-solid curve). Figure 13.a shows the fatigue data without shielding correction, while the effect of the average shielding is included in the data in Figure 13.b. Green markers are referred to the $\sqrt{area}$ of the specimen's killer defect measured from the approximated reference line. Black markers consider the whole envelope of the defect as far as the $\sqrt{area}$ is concerned. The yellow-filled squares are the three specimens of series D that were XCT scanned before testing. The $\sqrt{area}$ of these data-points is calculated based on the XCT reference line. As one may expect (after the LEVD discussion), the green markers are shifted on the left with respect to the black ones because a smaller defect size is considered when removing $R_{p,m}$ from the defect envelope. The XCT scans markers (more accurate size determination) are superposed to the green data-points. When the SIF range of experimental data is corrected by means the average shielding factor ($\overline{F} = 0.81$ for series D), all the data-points shift downwards consistently Figure 13.b. This means that the El-Haddad model can give an accurate prediction of the fatigue limit when the shielding correction is applied.

Knowing that our fatigue model is validated by experimental results, we can predict the fatigue limit starting from simple roughness parameters. The values of the predicted fatigue limit starting from $R_{v,max}$ parameter are listed in Table 13 for all the as-built series, where they are compared to the fatigue limit predicted from the $\sqrt{area}_{50\%}$ measured from the fractography images. The shielding correction is applied to both the cases, because we are focusing on the prediction in the endurance limit region.

Excellent predictions are performed taking $\sqrt{area}_{50\%}$ as initial defect size, with a relative percentage error with respect to the experimental results that is below 1% for the 4PB series and 5% for the axial series. The fatigue limit predictions from $\sqrt{10}\,R_{v,max}$ yield higher errors with respect to the experimental values but are excellent for the 4PB series (errors below 7%), while for the vertical series the error increases to the 17%.

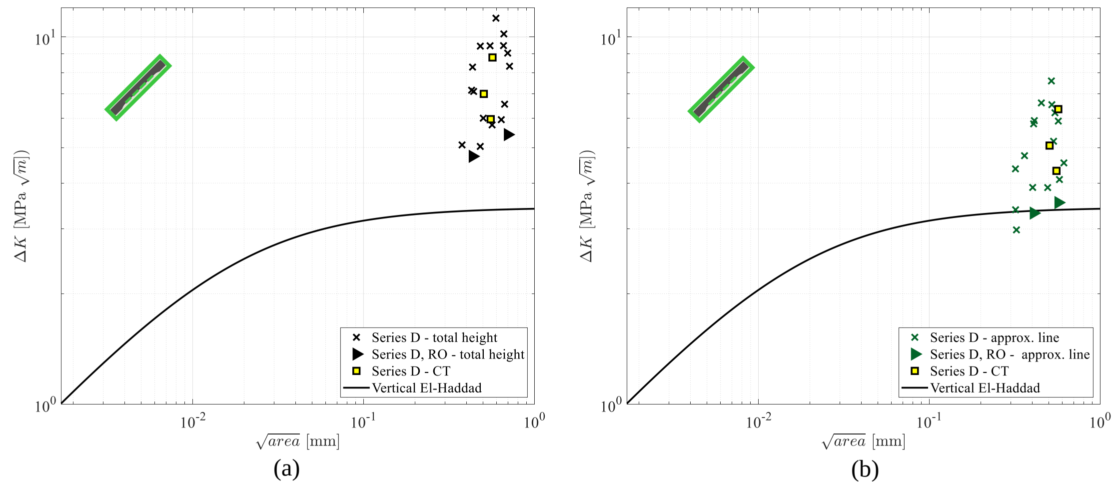

Figure 13: Kitagawa-Takahashi diagram of 4PB series D: a) Defect size measured with Total height method and no shielding correction; b) Defect size measured with reference to the Approximated mean line with shielding correction. In both the figures, the fatigue data when the defect size in terms of $\sqrt{area}$ is measured with the accurate XCT method are displayed as yellow squares.

Table 13: The experimental fatigue limit (first column on the left) compared to the fatigue limit predictions with shielding correction from killer defects' $\sqrt{area}_{50\%}$ and from profile roughness equivalent $\sqrt{10}\,R_{v,max}$.

Series / $\Delta\sigma_w$ [MPa]	**Experimental**	$\sqrt{area}_{50\%}$	$\sqrt{10}R_{v,max}$
Axial vertical	195	205	240
4PB - Series A	429	425	415
4PB - Series D	198	200	210
4PB - Series E	221	220	205

5.4. Prediction of the entire SN diagram

The fatigue life predictions were performed for each as-built series based on the tested specimens' defect size and morphology. Table 11 lists the initial crack size and aspect ratio that were introduced in the crack propagation algorithm for each series. The calculation of the SIF was performed according to the Wang and Lambert model for semi-elliptical cracks in finite thickness plates. The adopted crack growth model is based on the NASGRO equation at the stress ratio R=0.1. The failure condition considers a critical crack length of $3\,mm$ that corresponds to the 50% of the specimen's net section.

One important remark is that the NASGRO equation for $\Delta K_{th,LC}$ (Equation 6) considers a constant El-Haddad a_0 (in terms of crack length) parameter. In reality, a_0 should consider the load ratio R-dependence. For this reason, in the present crack propagation algorithm, the NASGRO equation 6 will be modified considering the specific El-Haddad parameter a_0 pertaining to the proper load ratio R calculated according to the Equation 14. The crack propagation was calculated assuming a semi-elliptical crack: the initial shape for each specimens's series was taken as the $(c/a)_{avg,in}$ value in Table 11.

The predicted stress-life curves for all the as-built series are shown in Figure 14. The colored-solid and the colored-dashed curves refer to life predictions performed considering the $\sqrt{area}_{50\%}$ defect size, without and with shielding correction, respectively. When the shielding correction is not applied, the finite-life zone of the predicted S-N curves is superposed to the experimental data, while the fatigue limit is underestimated (conservative estimation). When the correction is applied, the predicted fatigue limit increases as it considers the beneficial effect on the cracks' SIF induced by the interaction of the non-propagating cracks that started from surface notches that are close to each other.

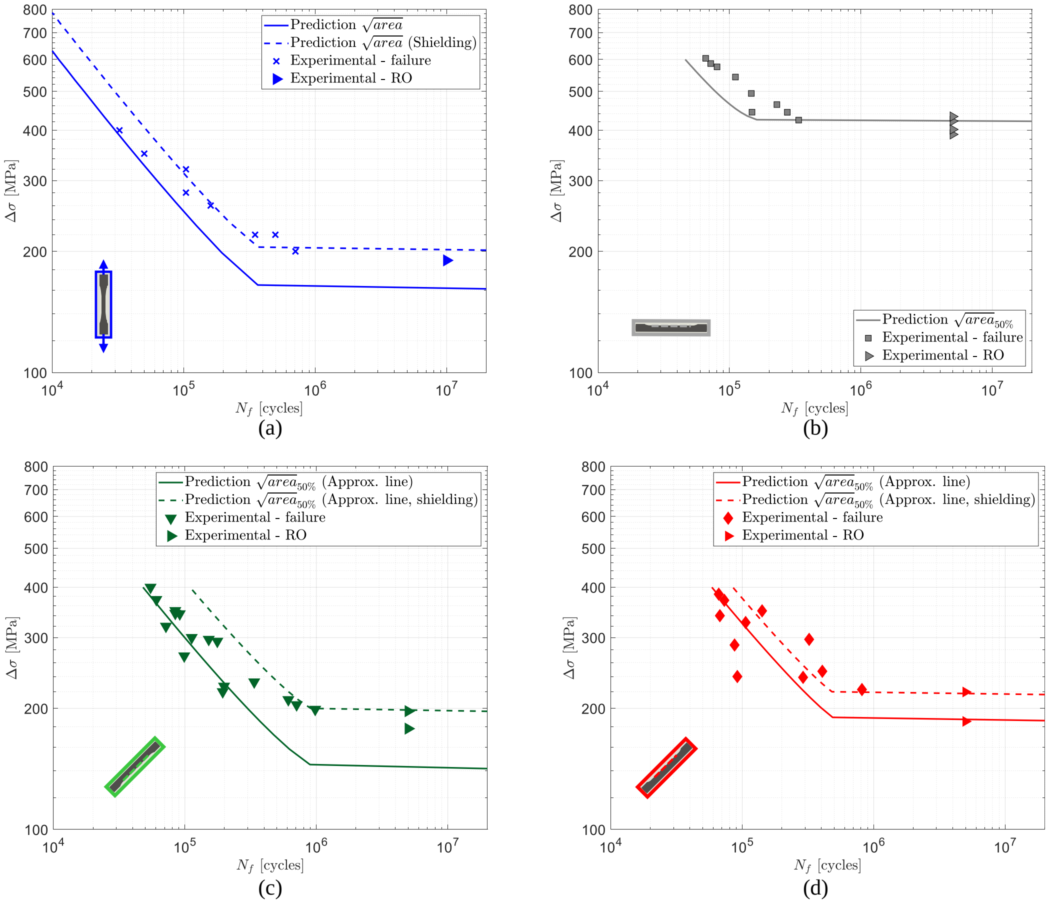

Figure 14: Stress-Life curve of axial and 4PB series predicted from defect size with 50% probability of occurrence with and without the shielding factor $\overline{F}$: a) Series axial (vertical), b) Series A (horizontal), c) Series D (downskin), d) Series E (upskin).

6. Discussion

This paper presents a comprehensive study on the fatigue performances of net-shape (as-built) LPBF surfaces differently orientated for the Ti6Al4V alloy. The work was structured to answer the following requests:

- Developing of a Fracture mechanics-based life prediction model which is capable to describe the crack propagation starting from the typical superficial features observed on the as-built surfaces.
- A methodology capable to pinpoint the size of the surface features leading to failure the fatigue specimens.
- Validating a shielding model that relies on roughness parameters, to be applied for the endurance limit estimation of rough parts.
- A proper roughness parameter to be used as an initial equivalent defect size for crack propagation calculations.

6.1. Fatigue model

It has been widely recognized in literature that a fatigue model based on the Kitagawa-Takahashi diagram is suitable to describe the endurance limit for as-built of L-PBF specimens printed at different orientations [20]. In this work, with the scope of predicting either the endurance limit and the finite-life region ($5 \cdot 10^4 < N_f < 5 \cdot 10^6$), we combined the El Haddad's short-crack model [65] and the NASGRO equation in a fracture mechanics-based crack growth model, which was developed considering the following key aspects. Firstly, it considers the load ratio R-dependence of the El-Haddad parameter $\sqrt{area_0}$ in the NASGRO equation. The short crack effect is then properly considered in the algorithm. Secondly, the crack driving force ΔK is calculated considering a shielding factor quantified separately from each orientation from the roughness parameters. The shielding model that is an input of the crack propagation algorithm was validated by means of experimental fatigue results (see Figure 13).

In this regard, the effect of the orientation is twofold, on one side it influences the roughness and then the size of the critical features, concurrently it also dictates the level of shielding. The validation of the fatigue model relies on an average equivalent defect size that is measured for each specimen orientation separately with a proper reference line as discussed in the following section.

6.2. Sizing of the critical superficial features and shielding effect

The need of an accurate definition of the reference line for the as-built surface depth measurements was highlighted. The reference line defines a boundary between the surface protrusions and the critical valleys such that a proper crack depth can be defined. Two methods have been proposed to position the reference line on the fracture surfaces (see Figure 10) both providing accurate results and thus reducing the scatter in the prediction with respect to the traditional "total height" measurement method [20].

It is worth observing that the fatigue strength of the present as-built (net-shape) specimens was dictated by the surface features and we did not observe internal or sub-surface defects leading to failure. The reason for this is that for the investigated specimens, the equivalent average surface defect ranges from approximately 40 microns to 500 microns. Only few sub-surface defects were detected on the fracture surfaces, but they were smaller than features at the fracture origin.

The transition to sub-surface initiation in general occurs when internal defects [66] and microstructural features (grain size, different phases) are larger than the surface ones (e.g. in VHCF tests [66–68]).

6.3. Shielding effect and life prediction

It is interesting to further analyze the life predictions performed with and without the shielding factor. The adoption of the shielding correction led to accurate prediction of the fatigue limit and to a non-conservative prediction (overestimation) of the life in the fatigue regime. This is due to the fact that the shielding effect is particularly important for non-propagating cracks (endurance limit region), while for a propagating crack (finite life region) it is expected that after the early stages of propagation, the crack tip will be less influenced by adjacent surface valleys.

The interpretation of this observation is given with the schematic reported in Figure 15. At high stress levels, even when several crack initiation spots are present on the surface, the smaller and slower cracks have no effect on the propagation of the major crack that propagates until the failure condition, being shielded by the presence of the other smaller cracks nearby only at the beginning of the propagation. Oppositely, at the fatigue limit, the presence of profile valleys, or even multiple non-propagating cracks close to each other, creates a shield on the crack driving force that hinders the propagation.

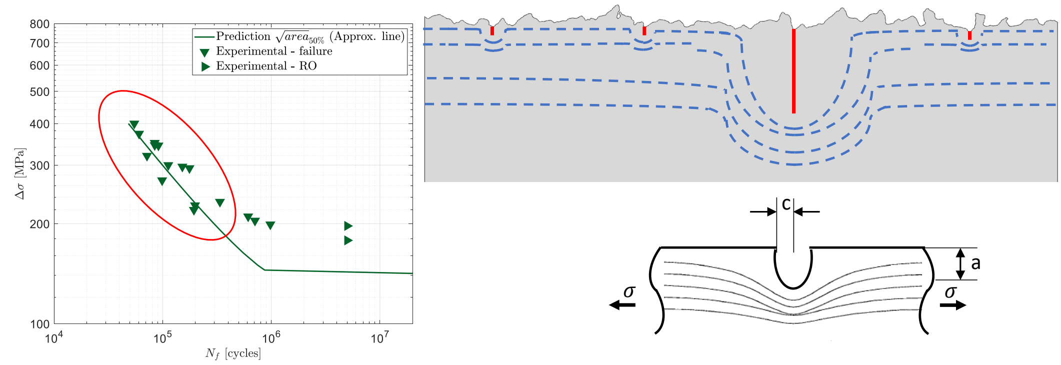

(a)

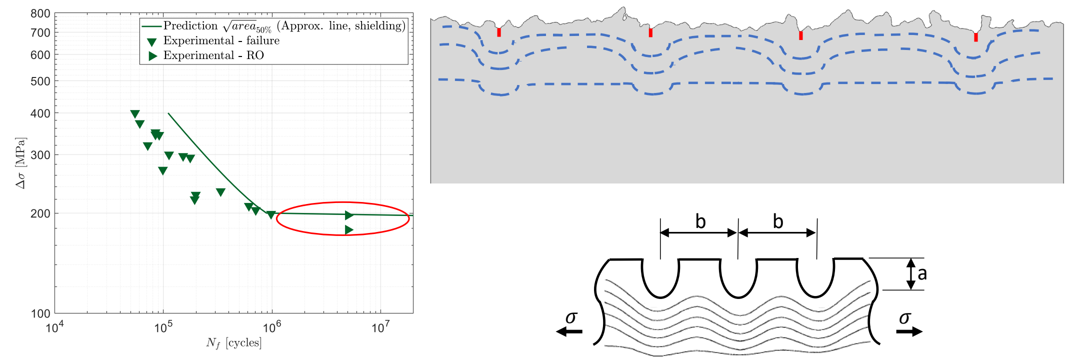

(b)

Figure 15: Different shielding behaviour in different fatigue life regions: a) In the finite-life region of the S-N curve the shielding phenomenon is not relevant, b) The shielding correction is needed in the fatigue limit region, due to the presence of several non-propagating cracks close to each other.

6.4. Roughness parameter for life calculations

In the second part of the paper we investigated the possibility to perform life predictions considering a roughness parameter as the initial equivalent defect size. Certainly, acquiring the reconstructed real geometry of the most loaded surface of the component could enable to spot the potential killer notch, but this operation is hindered by the feasibility of scanning at high resolution large and not fully accessible areas of the component. As an alternative, simple roughness measurements on test coupons printed at different orientations can be used for the prediction of the fatigue limit of an AM component, stated that the roughness parameter chosen as initial equivalent defect is fully representative of the surface morphology and correlates with the fatigue performances of the component. The adoption of the maximum valley roughness parameter $R_{v,max}$ as an equivalent shallow defect with a size $\sqrt{area} = \sqrt{10}R_{v,max}$ which is close to the average size of the surface killer defects found on as-built L-PBF surfaces (see Figure 12). The fatigue strength estimation obtained from roughness measurements, considering the shielding effect, were than similar to predictions based on the average size of surface features.

An open point for further research is to develop an extreme value statistics of the roughness parameter R_v to have a prospective valley parameter that allows to predict a lower-bound fatigue curve [69], as it is currently done for volumetric defects.

7. Conclusions

This study explored the impact of the as-built surface condition on the fatigue performance of an annealed L-PBF Ti6Al4V alloy through an experimental campaign on net-shaped fully-dense fatigue specimens printed in four different build orientations, with negligible impact of residual stresses and internal porosity. The main conclusions are herein summarized.

- The tests performed on the axial and 4PB specimens showed that the surface orientation has a paramount effect on the fatigue strength. The smooth surface condition (horizontal 4PB series A) leads to a consistent higher fatigue performance with respect to the roughest series (vertical axial and 4PB downskin series D).
- The observation of the fracture surfaces, the defect size analysis and the roughness analysis showed that the rough series (axial vertical, downskin D, upskin E) are characterized by deep surface grooves at the fracture origin, while the smooth horizontal series A by killer defects that are small-sized triangular-shaped surface micro-notches corresponding to the projections of the laser-weld tracks on the fracture plane. The axial series and the 4PB series E have intermediate defect sizes between the best-horizontal and worst-downskin cases.
- Roughness analyses from surface profiles were acquired with FV optical microscopy and XCT along the direction of the maximum principal stress. The maximum valley depth $R_{v,max}$ was found to be superposed to the LEVD distributions of the killer defects indicating that $R_{v,max}$ can be adopted as the initial equivalent defect size.
- The average roughness parameters $R_{v,m}$ and R_{sm} were used to calculate the average geometric factor $\overline{F}$ which is representative of the shielding behaviour for the as-built series.
- Fatigue life predictions for all the as-built series were performed by means of an algorithm based on the NASGRO equation and considering the average values of the killer defect sizes measured from the fracture surfaces. The introduction of the shielding factor $\overline{F}$ in the calculations was observed to yield accurate endurance limit estimations, while less precise predictions were obtained for the finite life region.
- Predictions of the endurance limit considering an initial equivalent defect size corresponding to $\sqrt{10}\,R_{v,max}$ are consistent with the experimental results and are in line with the predictions obtained from the average surface killer defects' size.

Acknowledgements

Authors acknowledge support by the Cleansky2 Project NEWTEAM (grant number 821274).

The authors would like to thank Leonardo S.p.A., in the person of Dr. Romano Iazurlo, for making available test data on vertical specimens tested at R=0.1.

Declaration of Competing Interest

The authors declare that they have no known competing financial interests or personal relationships that could have appeared to influence the work reported in this paper.

References

[1] E. Uhlmann, R. Kersting, T. B. Klein, M. F. Cruz, A. V. Borille, Additive Manufacturing of Titanium Alloy for Aircraft Components, Procedia CIRP 35 (2015) 55–60.

[2] P. Singh, H. Pungotra, N. S. Kalsi, On the characteristics of titanium alloys for the aircraft applications, Materials Today: Proceedings 4 (8) (2017) 8971–8982.

[3] A. N. Aufa, M. Z. Hassan, Z. Ismail, Recent advances in Ti-6Al-4V additively manufactured by selective laser melting for biomedical implants: Prospect development, Journal of Alloys and Compounds 896 (2022) 163072.

[4] J. J. Lewandowski, M. Seifi, Metal Additive Manufacturing: A Review of Mechanical Properties, Annual Review of Materials Research 46 (2016) 151–186.

[5] S. Liu, Y. C. Shin, Additive manufacturing of Ti6Al4V alloy: A review, Materials and Design 164 (2019) 107552.

[6] E. Wycisk, A. Solbach, S. Siddique, D. Herzog, F. Walther, C. Emmelmann, Effects of defects in laser additive manufactured Ti-6Al-4V on fatigue properties, Physics Procedia 56 (C) (2014) 371–378.

[7] S. Taylor, B. Jared, J. Koepke, E. Forrest, J. Beaman, Investigating applicability of surface roughness parameters in describing the metallic AM process, Solid Freeform Fabrication 2019: Proceedings of the 30th Annual International Solid Freeform Fabrication Symposium - An Additive Manufacturing Conference, SFF 2019 (2019) 1651–1664.

[8] S. Lee, J. W. Pegues, N. Shamsaei, Fatigue behavior and modeling for additive manufactured 304L stainless steel: The effect of surface roughness, International Journal of Fatigue 141 (2020).

[9] S. Lee, M. Muhammad, J. Zheng, S. Shao, N. Shamsaei, Locational dependency of additively manufactured parts : effects of surface roughness on fatigue behavior (2021).

[10] G. Nicoletto, Directional and notch effects on the fatigue behavior of as-built DMLS Ti6Al4V, International Journal of Fatigue 106 (August 2017) (2018) 124–131.

[11] G. Nicoletto, R. Konečna, M. Frkan, E. Riva, Influence of layer-wise fabrication and surface orientation on the notch fatigue behavior of as-built additively manufactured Ti6Al4V, International Journal of Fatigue 134 (October 2019) (2020).

[12] G. Strano, L. Hao, R. M. Everson, K. E. Evans, Multi-objective optimization of selective laser sintering processes for surface quality and energy saving, Proceedings of the Institution of Mechanical Engineers, Part B: Journal of Engineering Manufacture 225 (9) (2011) 1673–1682.

[13] G. Strano, L. Hao, R. M. Everson, K. E. Evans, Surface roughness analysis, modelling and prediction in selective laser melting, Journal of Materials Processing Technology 213 (4) (2013) 589–597.

[14] F. Cabanettes, A. Joubert, G. Chardon, V. Dumas, J. Rech, C. Grosjean, Z. Dimkovski, Topography of as built surfaces generated in metal additive manufacturing: A multi scale analysis from form to roughness, Precision Engineering 52 (2018) 249–265.

[15] J. C. Fox, S. P. Moylan, B. M. Lane, Effect of Process Parameters on the Surface Roughness of Overhanging Structures in Laser Powder Bed Fusion Additive Manufacturing, Procedia CIRP 45 (2016) 131–134.

[16] W. Eidt, E. P. Tatman, J. McCarther, J. Kastner, S. Gunther, J. Gockel, Surface roughness characterization in laser powder bed fusion additive manufacturing, Solid Freeform Fabrication 2019: Proceedings of the 30th Annual International Solid Freeform Fabrication Symposium - An Additive Manufacturing Conference, SFF 2019 (2019) 2165–2176.

[17] A. du Plessis, P. Sperling, A. Beerlink, O. Kruger, L. Tshabalala, S. Hoosain, S. G. le Roux, Standard method for microCT-based additive manufacturing quality control 3: Surface roughness, MethodsX 5 (September) (2018) 1111–1116.

[18] A. Yadollahi, N. Shamsaei, Additive manufacturing of fatigue resistant materials: Challenges and opportunities, International Journal of Fatigue 98 (2017) 14–31.

[19] J. Pegues, M. Roach, R. Scott Williamson, N. Shamsaei, Surface roughness effects on the fatigue strength of additively manufactured Ti-6Al-4V, International Journal of Fatigue 116 (April) (2018) 543–552.

[20] S. Beretta, M. Gargourimotlagh, S. Foletti, A. du Plessis, M. Riccio, Fatigue strength assessment of 'as built' AlSi10Mg manufactured by SLM with different build orientations, International Journal of Fatigue 139 (2020).

[21] T. Persenot, A. Burr, G. Martin, J. Y. Buffiere, R. Dendievel, E. Maire, Effect of build orientation on the fatigue properties of as-built Electron Beam Melted Ti-6Al-4V alloy, International Journal of Fatigue 118 (2019) 65–76.

[22] S. Lou, Z. Zhu, W. Zeng, C. Majewski, P. J. Scott, X. Jiang, Material ratio curve of 3D surface topography of additively manufactured parts: An attempt to characterise open surface pores, Surface Topography: Metrology and Properties 9 (1) (2021).

[23] D. Greitemeier, C. Dalle Donne, F. Syassen, J. Eufinger, T. Melz, Effect of surface roughness on fatigue performance of additive manufactured Ti-6Al-4V, Materials Science and Technology (United Kingdom) 32 (7) (2016) 629–634.

[24] Y. Murakami, K. Takahashi, T. Yamashita, Quantitative evaluation of the effect of surface roughness on fatigue strength (Effect of depth and pitch of roughness), Nippon Kikai Gakkai Ronbunshu, A Hen/Transactions of the Japan Society of Mechanical Engineers, Part A 63 (612) (1997) 1612–1619.

[25] R. Molaei, A. Fatemi, N. Sanaei, J. Pegues, N. Shamsaei, S. Shao, P. Li, D. H. Warner, N. Phan, Fatigue of additive manufactured Ti-6Al-4V, Part II: The relationship between microstructure, material cyclic properties, and component performance, International Journal of Fatigue 132 (2020).

[26] M. Nakatani, H. Masuo, Y. Tanaka, Y. Murakami, Effect of Surface Roughness on Fatigue Strength of Ti-6Al-4V Alloy Manufactured by Additive Manufacturing, Procedia Structural Integrity 19 (2019) 294–301.

[27] H. Masuo, Y. Tanaka, S. Morokoshi, H. Yagura, T. Uchida, Y. Yamamoto, Y. Murakami, Influence of defects, surface roughness and HIP on the fatigue strength of Ti-6Al-4V manufactured by additive manufacturing, International Journal of Fatigue 117 (April) (2018) 163–179.

[28] K. S. Chan, Characterization and analysis of surface notches on Ti-alloy plates fabricated by additive manufacturing techniques, Surface Topography: Metrology and Properties 3 (4) (2015).

[29] J. Zhang, A. Fatemi, Surface roughness effect on multiaxial fatigue behavior of additive manufactured metals and its modeling, Theoretical and Applied Fracture Mechanics 103 (2019).

[30] J. Gockel, L. Sheridan, B. Koerper, B. Whip, The influence of additive manufacturing processing parameters on surface roughness and fatigue life, International Journal of Fatigue 124 (October 2018) (2019) 380–388.

[31] S. Lee, B. Rasoolian, D. F. Silva, J. W. Pegues, N. Shamsaei, Surface roughness parameter and modeling for fatigue behavior of additive manufactured parts: A non-destructive data-driven approach, Additive Manufacturing 46 (May) (2021) 102094.

[32] A. du Plessis, S. Beretta, Killer notches: The effect of as-built surface roughness on fatigue failure in AlSi10Mg produced by laser powder bed fusion, Additive Manufacturing 35 (2020).

[33] C. A. Kantzos, R. W. Cunningham, V. Tari, A. D. Rollett, Characterization of metal additive manufacturing surfaces using synchrotron X-ray CT and micromechanical modeling, Computational Mechanics 61 (5) (2018) 575–580.

[34] G. Nicoletto, R. Konečná, M. Frkán, E. Riva, Surface roughness and directional fatigue behavior of as-built EBM and DMLS Ti6Al4V, International Journal of Fatigue 116 (April) (2018) 140–148.

[35] L. Barricelli, S. Beretta, Analysis of prospective SIF and shielding effect for cylindrical rough surfaces obtained by L-PBF, Engineering Fracture Mechanics 256 (oct 2021).

[36] N. Macallister, T. Hermann, Acta Materialia Fatigue life estimation of additively manufactured Ti-6Al-4V : Sensitivity , scatter and defect description in Damage-tolerant models, Acta Materialia 237 (2022).

[37] T. Persenot, A. Burr, R. Dendievel, J. Y. Buffière, E. Maire, J. Lachambre, G. Martin, Fatigue performances of chemically etched thin struts built by selective electron beam melting: Experiments and predictions, Materialia 9 (2020).

[38] M. J. Mian, J. Razmi, L. Ladani, Defect analysis and fatigue strength prediction of as-built Ti6Al4V parts, produced using electron beam melting (EBM) AM technology, Materialia 16 (September 2020) (2021) 101041.

[39] M. Simonelli, Y. Y. Tse, C. Tuck, On the texture formation of selective laser melted Ti-6Al-4V, Metallurgical and Materials Transactions A: Physical Metallurgy and Materials Science 45 (6) (2014) 2863–2872.

[40] G. Nicoletto, Anisotropic high cycle fatigue behavior of Ti-6Al-4V obtained by powder bed laser fusion, International Journal of Fatigue 94 (2017) 255–262.

[41] S. Cao, Y. Zou, C. V. S. Lim, X. Wu, Review of laser powder bed fusion (LPBF) fabricated Ti-6Al-4V: process, post-process treatment, microstructure, and property, Light: Advanced Manufacturing 2 (2) (2021) 1. doi:10.37188/lam.2021.020.

[42] S. Cao, R. Chu, X. Zhou, K. Yang, Q. Jia, C. V. S. Lim, A. Huang, X. Wu, Role of martensite decomposition in tensile properties of selective laser melted Ti-6Al-4V, Journal of Alloys and Compounds 744 (2018) 357–363. doi:10.1016/j.jallcom.2018.02.111.

[43] Q. Gaillard, S. Cazottes, X. Boulnat, S. Dancette, C. Desrayaud, Microstructure, texture and mechanical properties with raw surface states of Ti-6Al-4V parts built by L-PBF, Procedia CIRP 108 (C) (2022) 698–703.

[44] W. Xu, M. Brandt, S. Sun, J. Elambasseril, Q. Liu, K. Latham, K. Xia, M. Qian, Additive manufacturing of strong and ductile Ti-6Al-4V by selective laser melting via in situ martensite decomposition, Acta Materialia 85 (2015) 74–84.

[45] M. Carboni, L. Patriarca, D. Regazzi, Determination of ΔK_{th} by compression pre-cracking in a structural steel, Journal of ASTM International 6 (9) (2009). doi:10.1520/JAI102617.

[46] ASTM E647-13, Standard Test Method for Measurement of Fatigue Crack Growth Rates (2014).

[47] J. J. Lifton, T. Liu, Evaluation of the standard measurement uncertainty due to the ISO50 surface determination method for dimensional computed tomography, Precision Engineering 61 (2020) 82–92. doi:10.1016/j.precisioneng.2019.10.004.

[48] S. Carmignato, Accuracy of industrial computed tomography measurements: Experimental results from an international comparison, CIRP Annals - Manufacturing Technology 61 (1) (2012) 491–494.

[49] ISO - International Organization for Standardization, BS EN ISO 4288:1998. Geometrical Product Specifications (GPS) - Surface texture: Profile method - Rules and procedures for the assessment of surface texture, Geometrical product specifications (GPS) (1998).

[50] ISO - International Organization for Standardization, BS EN ISO 4287:1998. Geometrical product specification (GPS) - Surface texture : Profile method - Terms , definitions and surface texture parameters (2009).

[51] P. J. Scott, Feature parameters, Wear 266 (5-6) (2009) 548–551.

[52] J. Seewig, P. J. Scott, M. Eifler, B. Barwick, D. Hüser, Crossing - The-line segmentation as a basis for Rsm and Rc evaluation, Surface Topography: Metrology and Properties 8 (2) (2020).

[53] N. Senin, A. Thompson, R. K. Leach, Characterisation of the topography of metal additive surface features with different measurement technologies, Measurement Science and Technology 28 (9) (2017).

[54] S. Lee, S. Shao, D. N. Wells, M. Zetek, M. Kepka, N. Shamsaei, Fatigue behavior and modeling of additively manufactured IN718: The effect of surface treatments and surface measurement techniques, Journal of Materials Processing Technology 302 (October 2021) (2022) 117475.

[55] S. Wu, X-ray imaging of defect population and its effect on high cycle fatigue life of laser additive manufactured Ti6Al4V alloys X-ray imaging of defect population and its effect on high cycle fatigue life of laser additive manufactured Ti6Al4V alloys (May) (2022).

[56] ASTM E739-10, Standard Practice for Statistical Analysis of Linear or Linearized Stress-Life, Statistical Analysis of Fatigue Data 10 (Reapproved 2015) (2009) 129–129–9.

[57] S. Leuders, M. Thöne, A. Riemer, T. Niendorf, T. Tröster, H. A. Richard, H. J. Maier, On the mechanical behaviour of titanium alloy TiAl6V4 manufactured by selective laser melting: Fatigue resistance and crack growth performance, International Journal of Fatigue 48 (2013) 300–307.

[58] M. Tarik Hasib, H. E. Ostergaard, X. Li, J. J. Kruzic, Fatigue crack growth behavior of laser powder bed fusion additive manufactured Ti-6Al-4V: Roles of post heat treatment and build orientation, International Journal of Fatigue 142 (2021).

[59] G. Marci, Fatigue crack growth threshold concept and test results for Al- and Ti-alloys, ASTM Special Technical Publication (1372) (2000) 81–95.

[60] P. Edwards, M. Ramulu, Effect of build direction on the fracture toughness and fatigue crack growth in selective laser melted Ti-6Al-4V, Fatigue and Fracture of Engineering Materials and Structures 38 (10) (2015) 1228–1236. doi:10.1111/ffe.12303.

[61] V. Cain, L. Thijs, J. Van Humbeeck, B. Van Hooreweder, R. Knutsen, Crack propagation and fracture toughness of Ti6Al4V alloy produced by selective laser melting, Additive Manufacturing 5 (2015) 68–76.

[62] C. Rans, J. Michielssen, M. Walker, W. Wang, L. t. Hoen-Velterop, Beyond the orthogonal: on the influence of build orientation on fatigue crack growth in SLM Ti-6Al-4V, International Journal of Fatigue 116 (2018) 344–354.

[63] Murakami Y, Effects of Small Defects and Nonmetallic Inclusions, in: Metal Fatigue, 2002.

[64] E. Gumbel, Statistics of Extremes, Columbia University Press,(New York, NY:), 1958.

[65] M. H. El Haddad, K. N. Smith, T. H. Topper, Fatigue crack propagation of short cracks, Journal of Engineering Materials and Technology, Transactions of the ASME 101 (1) (1979) 42–46.

[66] K. Solberg, S. Guan, S. M. J. Razavi, T. Welo, K. C. Chan, F. Berto, Fatigue of additively manufactured 316l stainless steel: The influence of porosity and surface roughness, Fatigue & Fracture of Engineering Materials & Structures 42 (9) (2019) 2043–2052.

[67] G. Qian, Y. Li, D. Paolino, A. Tridello, F. Berto, Y. Hong, Very-high-cycle fatigue behavior of ti-6al-4v manufactured by selective laser melting: Effect of build orientation, International Journal of Fatigue 136 (2020) 105628.

[68] A. Tridello, J. Fiocchi, C. Biffi, G. Chiandussi, M. Rossetto, A. Tuissi, D. Paolino, Effect of microstructure, residual stresses and building orientation on the fatigue response up to 109 cycles of an slm alsi10mg alloy, International Journal of Fatigue 137 (2020) 105659.

[69] S. Beretta, More than 25 years of extreme value statistics for defects: Fundamentals, historical developments, recent applications, International Journal of Fatigue 151 (2021) 106407.

Highlights

- We have shown how to calculate the size of surface features in as-built AM surfaces;
- a detailed verification of the shielding effect by comparing the effective driving force with the ΔK_{th};
- the effect of shielding is more pronounced on the fatigue limit.

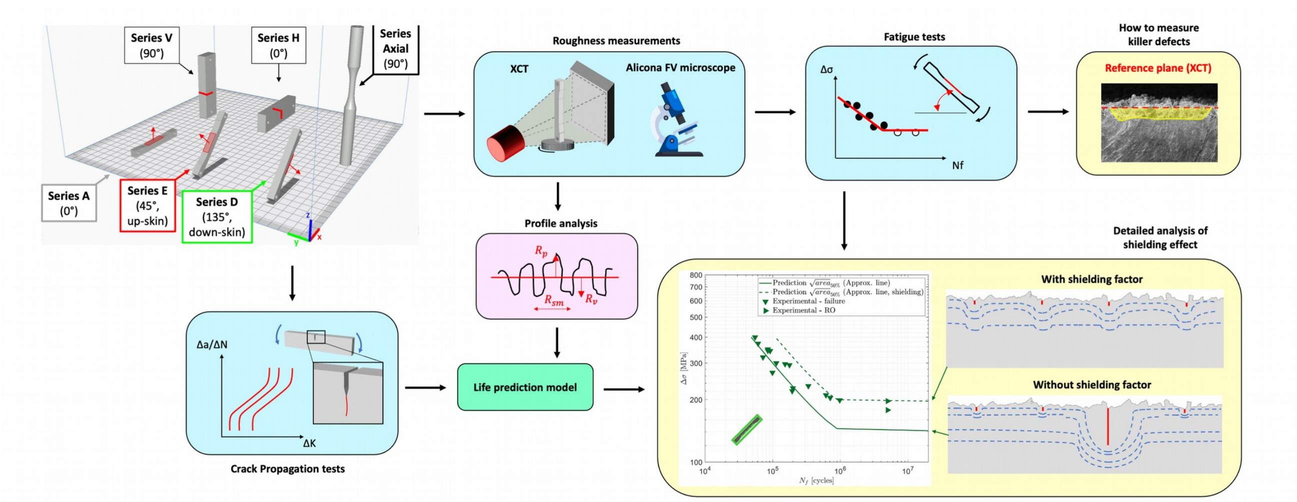

Series V
(90°)
Series H
(0°)
Series Axial
(90°)
Series A
(0°)
Series E
(45°, up-skin)
Series D
(135°, down-skin)
Roughness measurements
XCT
Alicona FV microscope
Fatigue tests
Δσ
Nf
How to measure killer defects
Reference plane (XCT)
Profile analysis
Detailed analysis of shielding effect
With shielding factor
Without shielding factor
Δa/ΔN
ΔK
Crack Propagation tests
Life prediction model

Declaration of interests

☐ The authors declare that they have no known competing financial interests or personal relationships that could have appeared to influence the work reported in this paper.

☒ The authors declare the following financial interests/personal relationships which may be considered as potential competing interests:

Stefano Beretta reports financial support was provided by European Commission. Stefano Beretta reports a relationship with European Commission that includes: funding grants.